

Dynamics of Vortex Dipoles in Anisotropic Bose–Einstein Condensates*

Roy H. Goodman[†], P. G. Kevrekidis[‡], and R. Carretero-González[§]

Abstract. We study the motion of a vortex dipole in a Bose–Einstein condensate confined to an anisotropic trap. We focus on a system of ODEs describing the vortices’ motion, which is in turn a reduced model of the Gross–Pitaevskii equation describing the condensate’s motion. Using a sequence of canonical changes of variables, we reduce the dimension and simplify the equations of motion. We uncover two interesting regimes. Near a family of periodic orbits known as guiding centers, we find that the dynamics is essentially that of a pendulum coupled to a linear oscillator, leading to stochastic reversals in the overall direction of rotation of the dipole. Near the separatrix orbit in the isotropic system, we find other families of periodic, quasi-periodic, and chaotic trajectories. In a neighborhood of the guiding center orbits, we derive an explicit iterated map that simplifies the problem further. Numerical calculations are used to illustrate the phenomena discovered through the analysis. Using the results from the reduced system, we are able to construct complex periodic orbits in the original, PDE, mean-field model for Bose–Einstein condensates, which corroborates the phenomenology observed in the reduced dynamical equations.

Key words. vortex dynamics, nonlinear Schrödinger equation, Gross–Pitaevskii equation, Bose–Einstein condensates, Hamiltonian ODEs

AMS subject classifications. 34A34, 34C15, 35Q55, 76M23, 76A25

DOI. 10.1137/140992345

1. Introduction. An atomic Bose–Einstein condensate (BEC) is a state of matter occurring only at extremely low temperatures. It is a gas composed of atoms (typically alkali atoms that behave as bosons) which, near absolute zero, lose their individual identity and share a single macroscopic wave function. The wavefunction of the cloud of BEC particles obeys the Gross–Pitaevskii (GP) equation, namely, the cubic nonlinear Schrödinger equation with an added external potential used for confining the atoms. BECs are inherently three-dimensional,

*Received by the editors October 21, 2014; accepted for publication (in revised form) by B. Sandstede February 14, 2015; published electronically April 14, 2015. The work of PGK and RCG was partially supported by NSF-DMS-0806762 and NSF-DMS-1312856.

<http://www.siam.org/journals/siads/14-2/99234.html>

[†]Department of Mathematical Sciences, New Jersey Institute of Technology, University Heights, Newark, NJ 07102 (goodman@njit.edu). The work of this author was supported by NSF-DMS-0807284.

[‡]Department of Mathematics and Statistics, University of Massachusetts, Amherst, MA 01003-4515, and Center for Nonlinear Studies and Theoretical Division, Los Alamos National Laboratory, Los Alamos, NM 87544 (kevrekid@math.umass.edu). The work of this author was partially supported by the Alexander von Humboldt Foundation, the Binational Science Foundation under grant 2010239, NSF-CMMI-1000337, FP7, Marie Curie Actions, People, International Research Staff Exchange Scheme (IRSES-605096), and the US-AFOSR under grant FA9550-12-10332. This author acknowledges the hospitality of the Center for NonLinear Studies at the Los Alamos National Laboratory during the final stages of this work; his work at the Los Alamos National Laboratory is supported in part by the U.S. Department of Energy.

[§]Nonlinear Dynamical System Group (<http://nlds.sdsu.edu>), Computational Science Research Center (<http://www.csrc.sdsu.edu>), and Department of Mathematics and Statistics, San Diego State University, San Diego, CA 92182-7720 (rcarretero@mail.sdsu.edu).

although strong confinement in one or two directions can effectively render the BEC two- or even one-dimensional. In nondimensional units (see, e.g., [18] for a discussion of the relevant adimensionalization), a cloud of repulsive BEC particles confined in a quasi-two-dimensional trap is described by the GP equation

$$(1.1) \quad iu_t = -\frac{1}{2}\Delta u + |u|^2 u + V(x, y)u,$$

where $u(x, y, t)$ is the BEC wavefunction—whose observable in the experiments is its associated density $|u|^2$ —and the potential $V(x, y)$ contains the effects of externally applied magnetic and optical fields which are used to trap the condensate at a particular location in space. In most studies, $V(x, y)$ is taken to be isotropic about the origin; yet, in a few more recent studies, the *critical* potential role of anisotropy in $V(x, y)$ has been investigated. The current study uses methods from Hamiltonian perturbation theory to gain a deeper understanding of the effects this anisotropy can have on the dynamics.

We note that this anisotropy is entirely straightforward to implement in ongoing experiments (see relevant discussion below) by means of the detailed available control over the magnetic traps that typically are used to induce the parabolic confinement [44, 45].

Like an ordinary inviscid fluid, the BEC flow may possess highly localized vortex lines or, if confined in a quasi-two-dimensional geometry, localized vortices. These may be idealized as point vortices, in which the vorticity is nonzero only at the vortex's center. Following a closed curve that encircles exactly one such vortex, one finds the phase of the wavefunction to have increased, or decreased, by 2π (or multiples thereof); this quantization of the circulation is, arguably, the most fundamental difference between the superfluid BEC vortices and those of an ordinary inviscid fluid. In order for a smooth solution of (1.1) to support a phase singularity, u must vanish at the point vortex core. Notice, in addition, the freedom in the clockwise or counterclockwise nature of the phase rotation (mirrored in the, respectively, negative or positive charge of the vortex).

The first experimental observation of vortices in atomic BECs [31] by means of a phase-imprinting method between two hyperfine spin states of an ^{87}Rb BEC [58] paved the way for a systematic investigation of their dynamical properties. Stirring the BECs [29] above a certain critical angular speed [28, 48, 52] led to the production of a few vortices [28] and even of robust vortex lattices [47]. Other vortex-generation techniques were also used in experiments, including the breakup of the BEC superfluidity by dragging obstacles through the condensate [41], as well as nonlinear interference between condensate fragments [49]. In addition, apart from unit-charged vortices, higher-charged vortex structures were produced [24] and their dynamical (in)stability was examined.

1.1. Recent precedents. Although much of this earlier work was focused on single vortices (or large clusters of vortices constituting vortex lattices), recently, a lot of attention has been paid to the problem of the motion that arises when a few vortices (i.e., small clusters) interact. These studies were partially seeded by the use of the so-called Kibble–Zurek mechanism in order to quench a gas of atoms from well above to well below the BEC transition in the work of [57]. The result of this was that phase gradients would not have sufficient time to “heal,” as would happen by adiabatically crossing the transition, but would rather often freeze, resulting in the formation of vortices and even multivortices. Subsequently, a

technique was devised that enabled for the first time the systematic dynamical visualization of such “nucleated” vortices [9] and even of vortex pairs, i.e., dipoles consisting of two oppositely charged vortices. The technique involved pulsing a microwave beam through the BEC that would expel a small fraction of it that could be imaged. This, in turn, spearheaded further studies [34, 56] which developed particle models that predicted the dipole dynamics (equilibria, near-equilibrium epicyclic precessions, and far from equilibrium quasi-periodic motions) observed in these experiments. A nearly concurrent development produced such vortex dipoles (one or multiple) by the superfluid analogue of dragging a cylinder through a fluid [40]. The role of the cylinder here was played by a laser beam. More recently, use of the above visualization scheme [9] together with rotation has made it possible to “dial in” and observe the dynamics of vortex clusters of, controllably, any number of vortices between 1 and 11 [39]. This led to the observation that such configurations may suffer symmetry-breaking events. As a result, instead of the commonly expected antidiagonal pair, equilateral triangle, or square configurations, it is possible to observe symmetry-broken configurations featuring asymmetric pairs, isosceles triangles, and rhombi or general/asymmetric quadrilaterals [60]. To further add to these developments, yet another experimental group [50] produced 3-vortex configurations but of alternating charge in the form of a tripole (i.e., a positive-negative-positive or its opposite).

Naturally, this considerable volume of experimental developments has triggered a number of corresponding theoretical efforts. Again, as for ordinary fluids, it is possible to derive a finite-dimensional system of ODEs that describes the motion of these vortices, in which each vortex induces a velocity field, and each vortex moves under the velocity field induced by the other vortices. Numerical studies have shown that the motion of vortices evolving under the GP equation (1.1) is mimicked by the motion arising in the ODE dynamics [25, 39, 54, 55, 60]. Analysis of the ODE system, displayed below in (2.1), has allowed for the prediction of many different dynamical phenomena in the GP equation, but also detailed numerical computations have been systematically used to unravel the evolution of these few vortex clusters [21, 38].

For example, Torres et al. [56] examined the *vortex dipole* consisting of two counterrotating vortices of equal and opposite vorticity, showing the existence of fixed points, in which the two vortices sit stably at a fixed distance on opposite sides of the magnetic trap’s center. They additionally found periodic orbits in which the two vortices travel at constant angular velocity around a circle centered at the trap’s center, keeping an angle of 180 degrees between them. Both of these types of orbits, known as guiding centers, are shown to be neutrally stable. Finally, they found families of quasi-periodic orbits, or, more specifically, relative periodic orbits. These solutions appear periodic when viewed in an appropriate rotating reference frame, so that in the laboratory reference frame, these orbits display whirls upon whirls (i.e., epitrochoidal motion).

Other studies [39, 60] have looked at small systems of two to four corotating vortices. The same types of solutions, such as relative stationary and relative periodic solutions, are found. However, the stationary and periodic solutions are shown to lose stability in Hamiltonian pitchfork bifurcations that result in the creation of new solutions in which the symmetry of the solutions is broken, even in the absence of anisotropy. The case of three vortices but with opposite charges (i.e., two positive and one negative or vice-versa) has also been a focal point of recent interest [20, 23], due especially to its potential for chaotic dynamics.

An additional direction that has been receiving a fair amount of interest is that of imposing asymmetries on the potential V . For instance, McEndoo and Busch [32] use a variational method to study the existence and stability of steady arrangements of small numbers of vortices in an anisotropic trap. They find that above a critical level of anisotropy the ground state arrangement undergoes a bifurcation, from a lattice in the isotropic case to a linear arrangement along the major axis of the anisotropic trap. Subsequently, the same authors explored the vortex dynamics in such anisotropic traps [33]. Stockhofe et al. [54, 55] showed that of the one-parameter family of stationary arrangements of a vortex dipole, only two survive the imposition of anisotropy: the arrangement with both vortices along the minor axis of the trap is always unstable, while the arrangement along the major axis is stable for small anisotropy but destabilizes when the anisotropy is increased beyond some threshold. This conclusion is then generalized to larger clusters of vortices. It is the dynamics that arises in the presence of small anisotropy that will be the systematic focus of the present study.

1.2. Organization of article. The remainder of the article is organized as follows. Section 2 introduces the differential equations and their Hamiltonian form. A change of variables is made that reduces the equations by one degree of freedom in the case of zero anisotropy. This isotropic reduced equation is studied in detail in section 3. This is very similar to work in [39, 60], but the reduction allows us to understand the solutions more thoroughly. In section 4 we derive a further reduced ordinary differential system that explains the effects of anisotropy very clearly. We then sketch the derivation of a separatrix map for this system, simplifying the dynamics further and allowing us to explain the various families of periodic orbits that arise due to the anisotropy. Section 5 contains the results of numerical simulations, including studies of the ODEs of vortex motion, and a bifurcation diagram based on the separatrix map. In section 6 we use the results obtained for the reduced ODE to construct complex periodic solutions for the original PDE, the GP equation. Here, despite the apparent complexity of the orbits, good correspondence is found between the ODE and the PDE findings. Finally, we discuss the impact of this work and future directions in section 7.

2. Mathematical formulation. Although our principal focus will be on the study of the ODEs, as indicated above the results will be corroborated by full numerical simulations of the PDE of the GP type from which these ODEs are derived (see section 6). This derivation can be obtained in a wide variety of ways. In the mathematical literature, it can be obtained by reverting to the semiclassical limit of the GP equation (i.e., the limit of large density, using as a small parameter the inverse of the density) and applying a variational approach [42], or by means of moment methods [17, 22] (by suitably decomposing the field), or through techniques based on the Fredholm alternative [4]. All of these techniques derive effective equations for the vortices as particles which incorporate two crucial features: the rotation of the vortices in the (here, anisotropic) trap and the pairwise velocity-field induced interactions between the vortices. On the physical side, there have also been numerous derivations of such equations both in the isotropic setting (see, e.g., [3]; for relevant reviews see [6, 7], and for a recent extension summarizing earlier literature see [8]) and even in the anisotropic [32] setting, based chiefly on applying variational methods to a suitable vortex-bearing ansatz.

2.1. Equations of motion and fixed points. A cluster of N vortices in an anisotropic BEC confined in a magnetic trap satisfies the ODEs

$$(2.1) \quad \begin{aligned} \dot{x}_k &= -s_k Q \omega_y^2 y_k + \frac{B}{2} \sum_{j \neq k} s_j \frac{y_j - y_k}{\rho_{jk}^2}, \\ \dot{y}_k &= s_k Q \omega_x^2 x_k - \frac{B}{2} \sum_{j \neq k} s_j \frac{x_j - x_k}{\rho_{jk}^2} \quad \text{for } k = 1, \dots, N, \end{aligned}$$

where (x_k, y_k) gives the Cartesian coordinates of the k th vortex, $s_k = \pm 1$ is its charge, and $\rho_{jk}^2 = (x_j - x_k)^2 + (y_j - y_k)^2$. By rescaling the independent and dependent variables, we may set $Q\omega_x^2 = 1$ and $Q\omega_y^2 = 1 + \epsilon$ [6, 53]. We here consider the vortex dipole case: $N = 2$ with $s_1 = 1, s_2 = -1$. For the remainder of the paper, we fix the parameter $B = 0.22$ describing the ratio of time-scales of rotation due to the vortex interactions and due to precession induced by the applied magnetic trap.¹ We work in the regime of weak anisotropy, namely, $\epsilon \ll 1$.

Remark 2.1. *The equations, as presented, contain the additional assumption that the vortices remain close to the trap's center. The full equations, in the case of isotropic traps, contain a modification to the precession frequency, i.e., an increase in the precession frequency as the outer rim of the condensate is approached; see, e.g., [19, 39, 60] for some of the implications of this modification. While we have not worked out the modified equations in the anisotropic case, we are here considering the leading-order effects of adding anisotropy and thus have reason to believe the simpler equations can provide insight into the general behavior; see also the relevant comparison between our ODE and PDE results below, which *a posteriori* justify the present considerations.*

It is shown in [56] that when $\epsilon = 0$, system (2.1) has a one-parameter family of fixed points (i.e., a resonance) of the form

$$(2.2) \quad (x_1, x_2, y_1, y_2) = \frac{\sqrt{B}}{2} (\cos \theta, -\cos \theta, \sin \theta, -\sin \theta), \quad 0 \leq \theta < 2\pi,$$

in which the two vortices lie on opposite sides of, and are equidistant from, the origin. When $\epsilon \neq 0$, only four of the fixed points on the resonance survive. Letting $\vec{x} = (x_1, x_2, y_1, y_2)$, these fixed points are

$$(2.3) \quad \vec{x}_Y = \pm \sqrt{\frac{B}{4(1+\epsilon)}} \begin{pmatrix} 0 \\ 0 \\ 1 \\ -1 \end{pmatrix} \quad \text{and} \quad \vec{x}_X = \pm \frac{\sqrt{B}}{2} \begin{pmatrix} 1 \\ -1 \\ 0 \\ 0 \end{pmatrix}.$$

These solutions consist of orbits aligned on the y -axis (\vec{x}_Y) and the x -axis (\vec{x}_X). When $0 < \epsilon < 1$, the arrangement \vec{x}_X is stable and \vec{x}_Y is unstable, while when $\epsilon < 0$, the opposite is true. We will assume throughout, without loss of generality, that $\epsilon > 0$.

We will be concerned with the dynamics that accompany this symmetry-breaking perturbation. The primary tools will come from Hamiltonian mechanics.

¹This number is obtained as the ratio of two frequencies $\omega_{\text{vort}} \approx 0.005$ and $\omega_{\text{pr}} = 0.023$, associated, respectively, with intervortex interaction and individual vortex precession in [39].

2.2. The Hamiltonian formulation. Stockhofe [53] showed that this system is Hamiltonian with canonical position and momentum variables $q_k = x_k$ and $p_k = -s_k y_k$, respectively, and Hamiltonian

$$H(q, p) = \sum_{k=1}^N \left[q_k^2 + (1 + \epsilon)p_k^2 + \frac{B s_k}{4} \sum_{j=k+1}^N s_j \ln \rho_{jk} \right],$$

where $\rho_{jk}^2 = (q_j - q_k)^2 + (s_j p_j - s_k p_k)^2$. For the vortex dipole this reduces to

$$H = H_0 + \epsilon H_1 = \frac{1}{2} (p_1^2 + q_1^2 + p_2^2 + q_2^2) - \frac{B}{4} \log \left((p_1 + p_2)^2 + (q_1 - q_2)^2 \right) + \frac{\epsilon}{2} (p_1^2 + p_2^2).$$

We introduce two successive canonical changes of variables that clarify the dynamics while preserving the Hamiltonian structure. First, we define action-angle coordinates

$$q_j = \sqrt{2J_j} \cos \phi_j \quad \text{and} \quad p_j = \sqrt{2J_j} \sin \phi_j, \quad j = 1, 2,$$

which transforms the Hamiltonian into

$$\begin{aligned} H_0 &= J_1 + J_2 - \frac{B}{4} \log \left(J_1 + J_2 - 2\sqrt{J_1}\sqrt{J_2} \cos(\phi_1 + \phi_2) \right), \\ H_1 &= J_1 \sin^2(\phi_1) + J_2 \sin^2(\phi_2). \end{aligned}$$

Since H_0 depends on the angle variables only through the combination $(\phi_1 + \phi_2)$, we define the additional canonical change of variables

$$(2.4) \quad \theta_1 = -\phi_1 + \phi_2, \quad \theta_2 = \phi_1 + \phi_2, \quad \rho_1 = \frac{-J_1 + J_2}{2}, \quad \rho_2 = \frac{J_1 + J_2}{2},$$

which yields the Hamiltonian $H = H_0 + \epsilon H_1$, with

$$(2.5) \quad \begin{aligned} H_0 &= 2\rho_2 - \frac{B}{4} \log \left(\rho_2 - \sqrt{\rho_2^2 - \rho_1^2} \cos \theta_2 \right), \\ H_1 &= \rho_1 \sin \theta_1 \sin \theta_2 + \rho_2 (1 - \cos \theta_1 \cos \theta_2). \end{aligned}$$

It is this latter form that we will use.

Remark 2.2. *The proper limits on the new angle variables are $-2\pi \leq \theta_1 < 2\pi$ and $0 \leq \theta_2 < 4\pi$. Nonetheless the reduced Hamiltonian is 2π -periodic in these angles. The natural limits become important when inverting the change of variables (2.4) to obtain the vortex paths.*

3. Analysis of the unperturbed equation. We first set $\epsilon = 0$ and consider the dynamics due to the unperturbed Hamiltonian H_0 . In this limit, the variable θ_1 is cyclic: it does not appear in H_0 as a result of the rotation invariance of the underlying system, an invariance that is broken when $\epsilon \neq 0$. Thus, the angular momentum ρ_1 is an additional conserved quantity, in involution with H_0 so that H_0 is a completely integrable Hamiltonian. This conservation law is generic for isotropic traps. The interesting phenomena described in later sections result mainly from the breaking of this isotropy.

The reduced system obeys the ODEs

$$(3.1a) \quad \dot{\theta}_2 = 2 - \frac{(\sqrt{\rho_2^2 - \rho_1^2} - \rho_2 \cos \theta_2) B}{4 (\rho_2 \sqrt{\rho_2^2 - \rho_1^2} - (\rho_2^2 - \rho_1^2) \cos \theta_2)},$$

$$(3.1b) \quad \dot{\rho}_2 = \frac{B \sqrt{\rho_2^2 - \rho_1^2} \sin \theta_2}{4 \rho_2 - 4 \sqrt{\rho_2^2 - \rho_1^2} \cos \theta_2}.$$

The additional angle θ_1 satisfies the evolution equation

$$\dot{\theta}_1 = \frac{-B}{4} \frac{\rho_1 \cos \theta_2}{\rho_2 \sqrt{\rho_2^2 - \rho_1^2} - (\rho_2^2 - \rho_1^2) \cos \theta_2}.$$

The system (3.1) has a single equilibrium

$$(3.2) \quad (\theta_2^*, \rho_2^*) = \left(\pi, \sqrt{\rho_1^2 + \frac{B^2}{64}} \right).$$

In the laboratory frame, the overall angular velocity is

$$\Omega_1 \equiv \dot{\theta}_1 = \frac{16\rho_1}{B + \sqrt{B^2 + 64\rho_1^2}}.$$

Translating this back to the (x, y) coordinates gives

$$\begin{pmatrix} x_1 \\ x_2 \\ y_1 \\ y_2 \end{pmatrix} = \begin{pmatrix} \frac{1}{2} \sqrt{\sqrt{B^2 + 64\rho_1^2} - 8\rho_1} \cos \left(\frac{\Omega_1}{2}(t - t_0) \right) \\ -\frac{1}{2} \sqrt{\sqrt{B^2 + 64\rho_1^2} + 8\rho_1} \cos \left(\frac{\Omega_1}{2}(t - t_0) \right) \\ \frac{1}{2} \sqrt{\sqrt{B^2 + 64\rho_1^2} - 8\rho_1} \sin \left(\frac{\Omega_1}{2}(t - t_0) \right) \\ -\frac{1}{2} \sqrt{\sqrt{B^2 + 64\rho_1^2} + 8\rho_1} \sin \left(\frac{\Omega_1}{2}(t - t_0) \right) \end{pmatrix}.$$

Here, the two vortices trace circular orbits, with both vortices collinear with and on opposite sides of the origin. The circle of fixed points (2.2) is obtained by setting $\rho_1 = 0$. This family of periodic orbits forms a two-dimensional tube in \mathbb{R}^4 . When $\rho_1 \neq 0$, the direction of rotation depends on its sign. The circle with $\rho_1 = 0$, on which there is no motion, is called a resonance and is structurally unstable to symmetry-breaking perturbations.

Figure 1 shows the typical shape of the phase plane in the case $\rho_1 = 0$ (left) and $\rho_1 \neq 0$ (right). The case $\rho_1 = 0$ is simpler. All the orbits, which are traversed counterclockwise, form a nested set of closed curves encircling the fixed point at $(\theta_2, \rho_2) = (\pi, B/8)$ (see blue dot). This fixed point is known as a “guiding center” in the BEC literature [56]. The accessible phase space is $0 < \theta_2 < 2\pi$ and $\rho_2 > |\rho_1| \geq 0$, and system (3.1) shows the vector field to be singular at the boundaries. The singularity at the left and right boundaries is due to the impossibility of collisions between the vortices. The singularity along the bottom edge is simply that of polar coordinates.

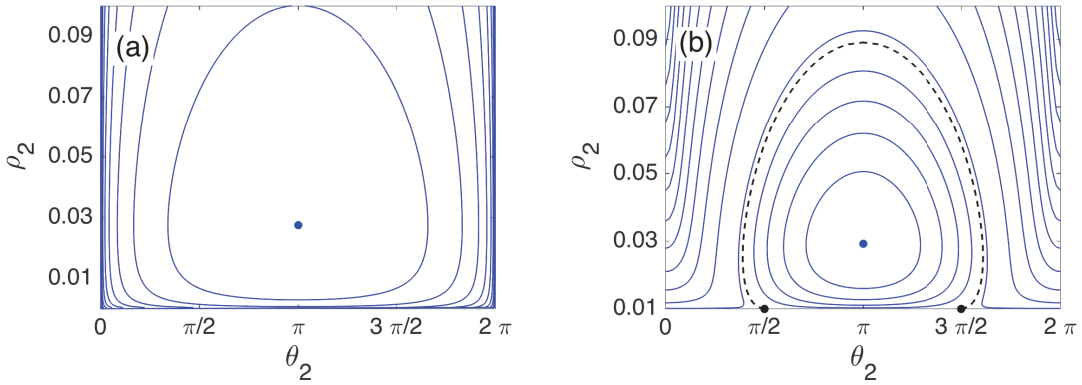


Figure 1. Phase plane of reduced system (3.1) with $B = 0.22$ with (a) $\rho_1 = 0$ and (b) $\rho_1 = 0.01$.

When $|\rho_1| > 0$, the left and right edges of the domain are no longer singular. The bottom edge remains singular, with two apparent hyperbolic fixed points at $\rho_2 = |\rho_1|$ and $\theta_2 = \pi/2$ or $3\pi/2$. These are not in fact fixed points or even relative fixed points in the (x, y) or (p, q) coordinate systems. At these points $\dot{\rho}_2 = 0$, but $\dot{\theta}_2$ is singular. When the solution reaches this point, one of the two vortices reaches the minimum of the trap, and its angular direction in the reduced coordinates, though not in the lab coordinates, jumps discontinuously.

The singularity may be removed by putting the right-hand side of $\dot{\rho}_2$ and $\dot{\theta}_2$ into (3.1) over common denominators. The system obtained by considering only the numerators of these expressions is nonsingular and has the same trajectories as system (3.1). In the desingularized system, these fixed points are hyperbolic. They are connected by three heteroclinic orbits—two along the line $\rho_2 = |\rho_1|$ (recalling the periodicity in the θ_2 direction) and a third extending into the region $\rho_2 > |\rho_1|$. The solutions near the elliptic fixed point oscillate counterclockwise, and those outside the separatrix move to the left. These points and their invariant manifolds play the same role as separatrices as they would if they were actual fixed points.

Each of the orbits in the phase planes of these systems is periodic in the (θ_2, ρ_2) coordinate system and quasi-periodic in the full (x, y) coordinates. The motion in (x, y) coordinates is complicated, but, because (θ_2, ρ_2) evolves independently of θ_1 , we may remove the θ_1 dependence from the solution entirely. We show such solutions in Figure 2. In the case $\rho_1 = 0$ all the solutions are in fact periodic. The fixed point of system (3.1) corresponds to the two vortices sitting along a line through the origin at equal distance from the origin. In the periodic orbit, the two vortices trace closed paths around these fixed points, the right vortex moving counterclockwise and the left orbit clockwise, satisfying $x_1 = -x_2$ and $y_1 = y_2$. The farther the orbits start from the fixed point, the closer they come to colliding.

When $\rho_1 \neq 0$, the motion is more complicated. The vortices can pass close to each other without colliding. There are two families of orbits with very different dynamics, corresponding to solutions exterior to or interior to the separatrix. These orbits are depicted in Figure 2(b) together with the separatrix (thick orbits). On the separatrix orbit one of the vortices crosses the origin, at which point its tangent direction changes discontinuously, as a result of the logarithmic singularity of H_0 .

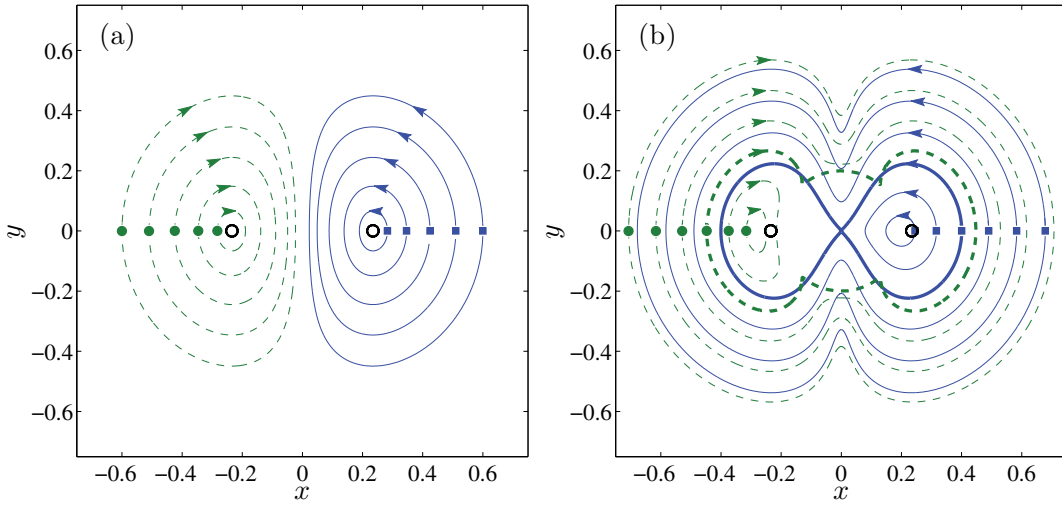


Figure 2. Typical orbits for two interacting vortices in an isotropic ($\epsilon = 0$) BEC. The solid blue line corresponds to the orbit of one vortex and the dashed green line to the orbit of the other vortex. Matching orbits for each pair correspond to the closest initial conditions (filled squares and circles) pairs from the origin. (a) Closed orbits of two vortices when $B = 0.22$ and $\rho_1 = 0$. At $t = 0$, the solutions start on the x -axis at maximal distance apart (see filled squares and circles). They rotate about their centers in opposing directions (see arrows indicating the direction of the orbits), nearly collide, and then move off again. (b) “Closed orbits” of the system with $\rho_1 = 0.01$, which are closed when viewed in an appropriate rotating reference frame. The orbits depicted with the thick lines correspond to the the separatrix in Figure 1(b). The solutions outside the separatrix cross the line $x = 0$ without colliding. The equilibrium positions (2.3) are depicted by the black empty circles.

Most of the above results are obtained by Torres et al. [56], although the reduced phase space provides a more global picture of the dynamics. The features not noticed in that study are the separatrix orbit and the corresponding orbits outside of this separatrix which encircle the origin and both fixed points (see Figure 2(b)). These authors use the more realistic model for the trap as discussed in Remark 2.1. It is straightforward to check that these features persist in the latter case.

4. Analysis of the perturbed system in a neighborhood of the resonance.

4.1. Change of variables and leading-order asymptotics. We can expect that when $\epsilon > 0$, there will be interesting dynamics near the resonance, which is given as the fixed point of the reduced system in (3.2). When $\epsilon > 0$, ρ_1 varies slowly, and so does ρ_2^* , which had been a fixed point. We introduce a further change of variables to fix this point at the origin by defining new variables $(\Theta_2, R_2) = (\theta_2 - \pi, \rho_2 - \rho_2^*)$. This is extended to the full four-dimensional system using the generating function [10] of type three²

$$F_3(\rho, \Theta) = -\Theta_2 \left(\rho_2 - \sqrt{\frac{B^2}{64} + \rho_1^2} \right) - \Theta_1 \rho_1 - \pi \rho_2.$$

²Recall that the angle variable θ_j is a position and the action variable ρ_j is a momentum.

This gives the implicit change of variables from (θ, ρ) to (Θ, R) :

$$\theta_j = -\frac{\partial F_3}{\partial \rho_j}, \quad R_j = -\frac{\partial F_3}{\partial \Theta_j}.$$

In terms of the new variables

$$\Theta_1 = \theta_1 + \frac{(\theta_2 - \pi)\rho_1}{\sqrt{\frac{B^2}{64} + \rho_1^2}}, \quad \Theta_2 = \theta_2 - \pi, \quad R_1 = \rho_1, \quad \text{and} \quad R_2 = \rho_2 - \sqrt{\frac{B^2}{64} + \rho_1^2},$$

the Hamiltonian takes the form

$$H = \frac{B}{4} \left(\beta + 8R_2 - \log \left(\sqrt{16R_2(\beta + 4R_2) + B^2} \cos \Theta_2 + \beta + 8R_2 \right) \right) \\ + \epsilon \left(\frac{1}{8} (\beta + 8R_2) \left(\cos \Theta_2 \cos \left(\Theta_1 - \frac{8\Theta_2 R_1}{\beta} \right) + 1 \right) - R_1 \sin \Theta_2 \sin \left(\Theta_1 - \frac{8\Theta_2 R_1}{\beta} \right) \right),$$

where $\beta = \sqrt{B^2 + 64R_1^2}$. Upon initial inspection, this form does not appear to be an improvement over the previous form of H . Its utility becomes apparent when we assume the trajectory remains in a neighborhood of the resonance, i.e., when R_1 , R_2 , and Θ_2 are small. A maximal balance is achieved by the assumptions

$$(4.1) \quad R_1 = O(\sqrt{\epsilon}), \quad R_2 = O(\sqrt{\epsilon}), \quad \text{and} \quad \Theta_2 = O(\sqrt{\epsilon}).$$

These make the leading-order Hamiltonian $O(\epsilon)$ and the perturbation $O(\epsilon^{3/2})$. The leading-order Hamiltonian then yields

$$H_{\text{approx}} = \frac{4}{B} R_1^2 + \frac{8}{B} R_2^2 + \frac{B}{16} \Theta_2^2 + \epsilon \left(\frac{B}{8} \cos \Theta_1 + R_2 + R_2 \cos \Theta_1 \right).$$

An additional canonical change of variables ($R_2 \rightarrow R_2 - \epsilon B/16$) removes one of the $O(\epsilon)$ terms while adding a new term at the ignored higher order, yielding

$$H_{\text{approx}} = \frac{4}{B} R_1^2 + \frac{8}{B} R_2^2 + \frac{B}{16} \Theta_2^2 + \epsilon \left(\frac{B}{8} \cos \Theta_1 + R_2 \cos \Theta_1 \right).$$

Using the above change of variables, we may rewrite the evolution equations as

$$(4.2a) \quad \ddot{\Theta}_1 - \epsilon \sin \Theta_1 - \frac{8\epsilon}{B} R_2 \sin \Theta_1 = 0,$$

$$(4.2b) \quad \ddot{R}_2 + 2R_2 + \frac{B\epsilon}{8} \cos \Theta_1 = 0.$$

This is quite a well-known system, and similar systems have been studied many times before using different methods. The model system consisting of a pendulum coupled to a harmonic oscillator goes back to Poincaré's seminal work on the geometric approach to mechanics [46] as described by Holmes [16]. A similar system was derived by Lorenz as a model of the "atmospheric slow manifold" [27] and subsequently analyzed by Camassa, Kovacic, and Tin [2],

who rigorously found some of the same features to be described below, but who stopped short of writing down an explicit iterated map like that identified below. A simple approach in which phase-plane analysis and matched asymptotics expansions are used to derive a discrete-time iterated map is developed in a series of papers by Goodman and Haberman [11, 13, 14]. In the final paper [11, section 7B], this system was reduced, formally, to a singular iterated map from the plane to itself. We briefly reiterate that calculation in the present context. We compare the analytical predictions of this approach with appropriate simulations of system (2.5) in section 5.3.

The appearance of a normal-form system (4.2) is a generic feature in the following sense. In the limit $\epsilon = 0$, the (Θ_2, R_2) equation corresponds to simple harmonic motion, and trajectories of this system are nested ellipses surrounding the origin. The other angle Θ_1 varies at a constant rate, and we may define a Poincaré map each time $\Theta_1 = 0 \bmod 2\pi$. The trajectories of this map lie on the same family of ellipses. For sufficiently small nonzero values of ϵ , KAM theory ensures that most of these ellipses persist, but those whose period is a rational multiple of the frequency $T_2 = 2\pi/\sqrt{2}$ of the (Θ_2, R_2) motion will break up into a sequence of fixed points of alternating elliptic and hyperbolic type. In a band containing these fixed points, the nonlinearity looks precisely like that of a pendulum [26].

4.2. Derivation of an iterated-map approximation. Clearly, taking $\epsilon \rightarrow 0$ naively in (4.2) yields an uncoupled system, so the limit must be taken carefully. To do this, scale time by $\tau = \sqrt{\epsilon}t$. In terms of this variable, dropping subscripts on R_2 and Θ_1 , and letting $(\cdot)'$ denote τ -derivatives, (4.2) is rescaled to

$$(4.3a) \quad \Theta'' - \sin \Theta - \frac{8}{B}R \sin \Theta = 0,$$

$$(4.3b) \quad R'' + \lambda^2 R + \frac{B}{8} \cos \Theta = 0,$$

with $\lambda^2 = 2/\epsilon$. Note that the coupling is now formally $O(1)$, but, because Θ and R evolve on such different time-scales, the energy transfer between the two modes is exponentially small. Temporarily setting $R = 0$, the first component conserves a pendulum-like energy

$$(4.4) \quad E = \frac{1}{2}\Theta'^2 + \cos \Theta - 1.$$

Because (4.3a) depends on $R(\tau)$, the energy E also evolves in time under the full dynamics of (4.3).

The map is constructed in consultation with Figure 3, which shows a numerical simulation of the equations of motion in form (4.3). Panel (a) shows $\Theta(\tau)$ and identifies a sequence of “transition times” τ_j at which $\Theta = \pi \bmod 2\pi$. We also define a sequence of “plateau times” t_j (not shown) satisfying $\tau_{j-1} < t_j < \tau_j$, defined as the times at which the solution makes its closest approach to the saddle point at $\Theta = 0 \bmod 2\pi$. Panel (b) shows that at the times τ_j , the energy undergoes a rapid jump between two plateaus. On the plateaus where $E < 0$, the solution librates, with zero net change of the angle over one period, while on those with $E > 0$, the solution rotates, with Θ changing monotonically by $\pm 2\pi$. Panel (c) shows the evolution of $R(\tau)$. The amplitude and phase of this oscillatory variable are different at each τ_j , and these

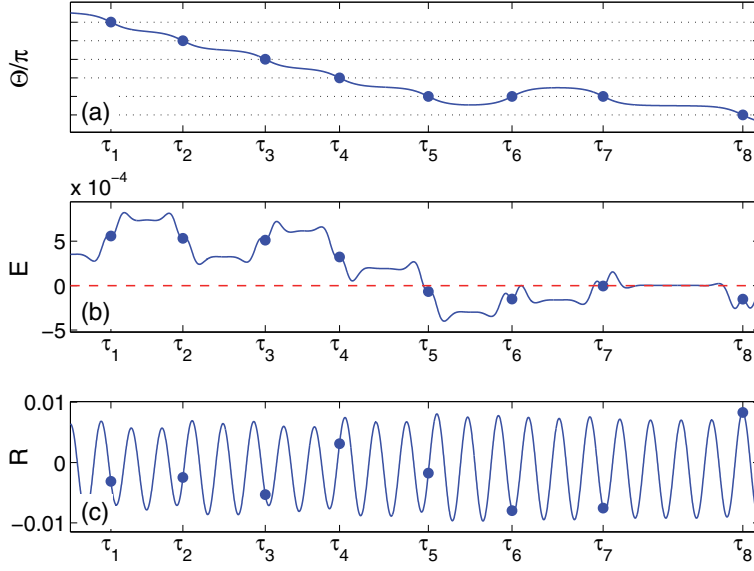


Figure 3. Figure used in constructing the iterated map. (a) $\Theta(\tau)$ with horizontal dashed lines at $\Theta = \pi \text{ mod } 2\pi$, the minima of the potential $V(\Theta) = \cos \Theta - 1$. This defines a sequence of times τ_j (see filled blue circles in all panels) at which $\Theta(\tau_j)$ reaches these minima. (b) The energy $E(\tau)$ in the pendulum-like component. (c) The evolution of the oscillatory variable $R(\tau)$.

change slightly at each transition time. The interval between transitions is longer on plateaus where E is near zero, so that $R(\tau)$ oscillates more on these periods.

We define E_j to be the plateau value of energy on the interval (τ_{j-1}, τ_j) and assume that on this interval

$$(4.5) \quad R = R_{\text{before}}(\tau) \approx -\frac{B}{8\lambda^2} + \mathcal{C} (c_j \cos \lambda(\tau - \tau_j) + s_j \sin \lambda(\tau - \tau_j)).$$

Although written in terms of the transition time τ_j , this represents the state of the system near the plateau time τ_j , where $\cos \Theta \approx 1$. The constant \mathcal{C} is chosen below to normalize the variables and eventually simplify the derived map, and c_j and s_j are the corresponding amplitudes for the cosine and sine components. Thus, we seek a map of the form $(E_{j+1}, c_{j+1}, s_{j+1}) = F(E_j, c_j, s_j)$. This is done for a very similar system in [11], so we include here only a brief sketch of the derivation, with somewhat less precise language.

The solution is approximated using a matched asymptotic expansion, alternating between “outer solutions” near the saddle points and “inner solutions,” along which the approximate solution is given by the heteroclinic trajectory $\Theta_H(\tau) = 4 \tan^{-1}(e^{\pm\tau})$. First, an approximate solution to (4.3b) satisfying condition (4.5) is given by variation of parameters:

$$(4.6) \quad \begin{aligned} R(\tau) &= R_{\text{before}}(\tau) - \frac{B \cos \lambda(\tau - \tau_j)}{8\lambda} \int_{-\infty}^{\tau} \sin \lambda(s - \tau_j) \cos (\Theta_H(s - \tau_j)) ds \\ &\quad + \frac{B \sin \lambda(\tau - \tau_j)}{8\lambda} \int_{-\infty}^{\tau} \cos \lambda(s - \tau_j) \cos (\Theta_H(s - \tau_j)) ds. \end{aligned}$$

In the limit $\tau \rightarrow \infty$, the first of the above integrals vanishes by symmetry, so as $\tau - \tau_j \rightarrow +\infty$

$$R(\tau) = R_{\text{after}}(\tau) \sim R_{\text{before}} + \frac{B \sin \lambda(\tau - \tau_j)}{8\lambda} \int_{-\infty}^{\infty} \cos \lambda(s - \tau_j) \cos (\Theta_H(s - \tau_j)) ds.$$

We define \mathcal{C} to be the coefficient of $\sin \lambda(\tau - \tau_j)$ in the above equation. Evaluating the integral by residues then gives

$$\mathcal{C} = \frac{B\pi}{4 \sinh \frac{\pi\lambda}{2}}.$$

This then simplifies the above formula to

$$(4.7) \quad R_{\text{after}}(\tau) = -\frac{B}{8\lambda^2} + \mathcal{C} (c_j \cos \lambda(\tau - \tau_j) + (s_j + 1) \sin \lambda(\tau - \tau_j)).$$

Next, the change in energy is calculated using

$$E_{j+1} - E_j = \int_I \frac{dE}{d\tau} d\tau = \int_I (\Theta_H''(\tau) - \sin \Theta_H) \Theta_H'(\tau) d\tau = \int_I \left(\frac{8}{B} R(\tau) \sin \Theta_H(\tau) \right) \Theta_H'(\tau) d\tau,$$

where E is given by (4.4) and I is the time interval $[\tau_j, \tau_{j+1}]$. The integral is approximated by replacing the interval I with the whole line and using the formula (4.6) for $R(\tau)$. Two more steps complete the calculation: the first is an integration by parts to move the τ derivative from $\Theta_H' \sin(\Theta_H)$ to R , and the second is a residue integral identical to that performed above. These lead to the following recurrence relationship for consecutive E values:

$$E_{j+1} = E_j - \frac{32\lambda^2 \mathcal{C}^2}{B^2} (1 + 2s_j).$$

Formula (4.7) is given in terms of $(\tau - \tau_j)$. To complete the specification of the map, we must rewrite it in terms of $(\tau - \tau_{j+1})$, and thus we need to find $(\tau_{j+1} - \tau_j)$. The matching procedure, described in detail in [11, sec. III], yields the expected result to leading order: it is the time between two successive approaches to $\Theta = \pi \bmod \pi$ along the periodic orbit of (4.3a) with R set to zero and energy E_{j+1} . This is found to be

$$\tau_{j+1} - \tau_j \approx \log \frac{32}{|E_{j+1}|}.$$

With this, we find

$$\begin{pmatrix} c_{j+1} \\ s_{j+1} \end{pmatrix} = \begin{pmatrix} \cos \psi_{j+1} & \sin \psi_{j+1} \\ -\sin \psi_{j+1} & \cos \psi_{j+1} \end{pmatrix} \begin{pmatrix} c_j \\ s_j + 1 \end{pmatrix}, \quad \text{where } \psi_{j+1} = \lambda(\tau_{j+1} - \tau_j).$$

Close inspection shows that the reduced discrete map conserves an energy

$$\mathcal{H} = \frac{B^2}{32\mathcal{C}^2 \lambda^2} E_j + (c_j^2 + s_j^2).$$

Using this energy, we may eliminate E_j and reduce the dimension of the map from three to two. Defining $Z_j = c_j + i(s_j - \frac{1}{2})$ and $\Psi(Z) = 2\lambda \log \frac{C\lambda}{B} + \lambda \log |Z|^2 - \mathcal{H}$, the map takes the particularly simple form $Z_{j+1} = \mathcal{F}(Z_j)$ with

$$(4.8) \quad \mathcal{F}(Z) = e^{-i\Psi(Z+\frac{i}{2})} \left(Z + \frac{i}{2} \right) + \frac{i}{2}.$$

The constant $-\frac{i}{2}$ used in defining Z_j is convenient because the inverse map now takes an almost identical form:

$$\mathcal{F}^{-1}(Z) = e^{i\Psi(Z-\frac{i}{2})} \left(Z - \frac{i}{2} \right) - \frac{i}{2}.$$

When $\mathcal{H} < 0$, the argument in the logarithm in the above functions is bounded below, but for $\mathcal{H} > 0$, the logarithmic term in $\mathcal{F}(Z)$ and, respectively, $\mathcal{F}^{-1}(Z)$, is singular on the circles

$$\Gamma_+ = \left\{ Z \in \mathbb{C} : \left| Z + \frac{i}{2} \right|^2 = \mathcal{H} \right\} \quad \text{and} \quad \Gamma_- = \left\{ Z \in \mathbb{C} : \left| Z - \frac{i}{2} \right|^2 = \mathcal{H} \right\}.$$

4.3. Interpretation of the maps. Further, let D_+ and D_- be the discs interior to these circles, and let D_+^c and D_-^c be their complements. The phase space of the map can have three different configurations depending on \mathcal{H} .

- *Configuration 1:* When $\mathcal{H} < 0$, the system has too little energy for the pendulum to rotate, and all solutions stay in the librating mode. The discs do not exist in this configuration.
- *Configuration 2:* For $0 < \mathcal{H} < \frac{1}{4}$, the discs are disjoint.
- *Configuration 3:* Finally, for $\frac{1}{4} < \mathcal{H}$, the two discs have nontrivial intersection.

In configuration 1, generalize the definitions of the disks to $D_+ = D_- = \emptyset$ and their complements $D_+^c = D_-^c = \mathbb{C}$. With this notation, if $Z_j \in D_-$, then the pendulum is outside the separatrix (rotating) on iterate j , whereas it is inside (librating) if $Z_j \in D_+^c$. Similarly, if $Z_j \in D_+$, the pendulum rotates on step $j+1$, and for $Z_j \in D_+^c$ it executes a libration at step $j+1$. In configuration 2, the empty intersection of the two disks indicates that at these energy levels, the pendulum mode can be in the rotational state for at most one iteration at a time before returning to the libration state, while in configuration 3, the solution may stay in the rotational mode arbitrarily long.

4.4. Fixed points and periodic points. As an example of the type of calculation that can be accomplished using this map, we note that fixed points of map (4.8) correspond to periodic orbits of the ODE system. Clearly, solutions to the fixed points of the map (4.8) satisfy $|Z_{j+1} - \frac{i}{2}| = |Z_j + \frac{i}{2}|$, so that a fixed point Z^* satisfies $Z^* = X \in \mathbb{R}$. Using this value in the map yields an implicit formula for these fixed points that can be solved numerically:

$$(4.9) \quad X = -\frac{1}{2} \cot \frac{\Psi \left(\sqrt{X^2 + \frac{1}{4}} \right)}{2}.$$

Note that $R(t)$ is assumed to be small enough that it satisfies a linear ODE, and that the magnitudes of $X(t)$ and $R(t)$ are of the same size up to the scaling constant C , but that

this equation has a countably infinite and unbounded family of solutions. Therefore, large solutions fail to satisfy assumption (4.1) and likely do not correspond to actual solutions of the ODE from which the map was derived.

We also find two families of period-two points. The first family, which we call type 1, consists of pairs of complex points Z_1 and Z_2 that are complex conjugates of each other: $Z_2 = \bar{Z}_1$. In the second family, type-2 period-two points, Z_1 and Z_2 are real, with $Z_2 = -Z_1$. Again, we can find explicit values of \mathcal{H} where these families arise in period doubling bifurcations. While we do not write down these families of solutions, we will draw a partial bifurcation diagram below in section 5.3.

5. Numerical experiments. We turn now to numerical studies, guided by the analysis presented above. We begin with two numerical simulations of the initial value problem, with initial conditions chosen to display behavior in the interesting regimes already identified. We then use Poincaré sections to place these simulations within a wider view of the dynamics, showing how chaotic dynamics coexists with periodic and quasi-periodic dynamics when the anisotropy parameter ϵ is nonzero. Finally, we discuss the bifurcations of periodic orbits based on the iterated map derived in section 4.2.

5.1. Initial-value problem simulations. Figure 1 shows two distinguished regions in the phase space of the isotropic $\epsilon = 0$ system: near the separatrix between librating and rotating periodic orbits and near the guiding center fixed point (θ_2^*, ρ_2^*) . By performing simulations with initial conditions near these regions, we are able to find interesting dynamics.

Near the separatrix. First, we show the dynamics in a neighborhood of the separatrix that exists when $\rho_1 \neq 0$. We initialize the solution with parameters $B = 0.22$ and $\epsilon = 0.2$, and with initial conditions close to the point $(\theta_2, \rho_2) = (3\pi/2, |\rho_1|)$, where the separatrix orbit leaves the bottom edge of the reduced phase diagram. The actual initial condition is $(\theta_1, \theta_2, \rho_1, \rho_2) = (4.7421, 4.7068, -0.0050, 0.0052)$, which lies on the energy level $H = 0.3$, for later reference. A portion of the projection of the phase plane onto the coordinates (θ_2, ρ_2) is shown in Figure 4. The solution jumps between the interior of the separatrix and the exterior several times, in a manner we show below to be chaotic.

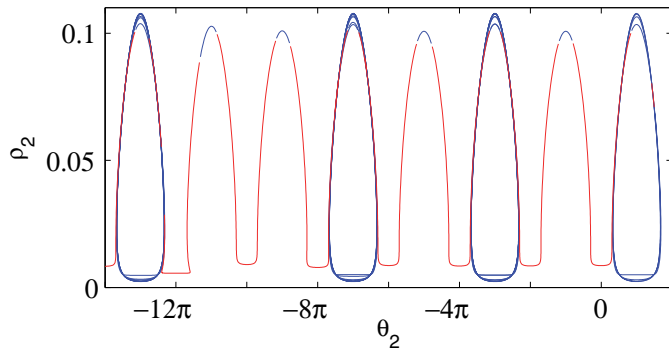


Figure 4. The (θ_2, ρ_2) component of the motion near the separatrix of Figure 1. The solution is plotted in red when the instantaneous energy $H_0(\theta_2, \rho_1, \rho_2)$ lies below the separatrix value and in blue when it lies above.

To explain the dynamics of the vortices, we show the solutions in the position variable

(x_1, x_2, y_2, y_2) obtained by undoing the repeated change of coordinates performed in section 2. A small portion of this numerical trajectory is shown in Figure 5(a). The dynamics is reminiscent of the $\epsilon = 0$, $\rho_1 = 0$ case shown in Figure 2(a). While that figure represents the relative motion of the vortices from a rotating reference frame, the present figure is in the fixed reference frame. In the unperturbed case, the two particles' positions are mirror images of each other across the y -axis, while for the perturbed problem, there is some small deviation from this symmetry. The perturbed orbits are chaotic and do not close. Occasionally one vortex or the other encircles the origin. This happens precisely when the position (θ_2, ρ_2) crosses to the outside of the separatrix shown in Figure 4.

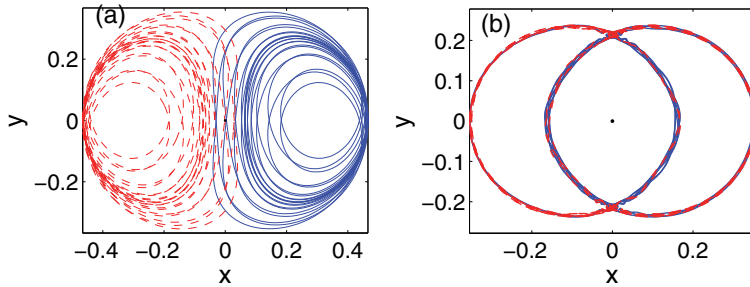


Figure 5. The reconstructed particle trajectories from (a) the near-separatrix orbit and (b) the near guiding center.

Near the guiding center. Figures 5(b) and 6 show a simulation of dynamics near the guiding-center fixed point. The parameters B and ϵ are as in the previous simulation, and the initial condition chosen is $(\theta_1, \theta_2, \rho_1, \rho_2) = (0.11, \pi, 0, 0.024)$, which lies close to an unstable fixed point of the Poincaré map described in the next section. In this figure, note that θ_1 switches chaotically between three behaviors: monotonically increasing, monotonically decreasing, and oscillating. The sign of ρ_1 is opposite that of $d\theta_1/dt$. Also note that $\theta_2 \approx \pi$ to within 0.15 radians (about 9°), and the variation of ρ_2 is much smaller than that of ρ_1 , indicating that the two vortices remain nearly collinear with, and on opposite sides of, the center of the magnetic trap. The phase-plane diagram shows that the (θ_1, ρ_1) dynamics stay close to what appears to be a pendulum separatrix, consistent with the reduced system (4.2).

Referring to the reconstruction of the laboratory-frame trajectories in Figure 5(b), we describe the dynamics of the two vortices. The vortices remain nearly opposite each other. When they approach the unstable solution \vec{x}_Y on the y -axis, they slow down. From the reduced system (4.2), the potential energy is high at this point, so the kinetic energy is small. Depending on their kinetic energy, they may either turn around or else may, after a pause, continue in the direction they were headed. Depending on which orientation they are rotating, one vortex will move on the “inside track” closer to the origin and the other along the “outside track.”

5.2. Poincaré sections. The results of a few initial-value simulations are insufficient to understand the dynamics and can be put into a better context by plotting Poincaré sections. We define the Poincaré section to be the set of intersections of a given trajectory with the hyperplane $\theta_2 = (2n + 1)\pi$ that cross with $\theta'_2(t) < 0$. This corresponds in the limiting case

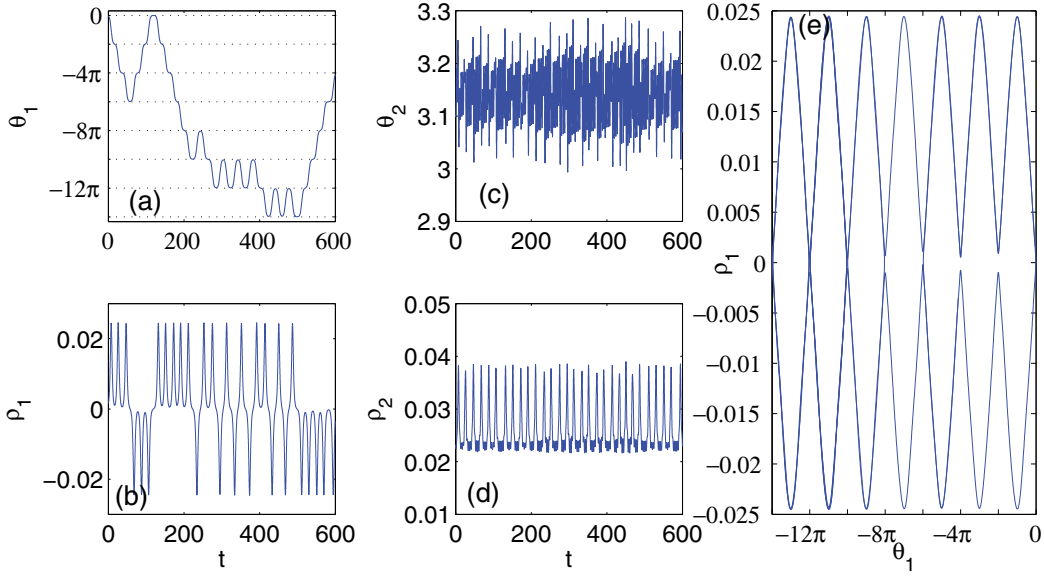


Figure 6. Numerical solution of initial value problem near the guiding center orbit. (a)–(d) Evolution of the components of the solution. (e) Phase portrait projected to (θ_1, ρ_1) coordinates.

$\epsilon = 0$ to a half-line extending upward from $\rho_2 = \rho_2^*$ in Figure 1. In order to plot multiple trajectories in the same figure, all trajectories must be chosen to lie on the same level set of the full Hamiltonian $H^* = H(\theta, \rho; \epsilon)$. Taking (θ_1, ρ_1) as parameterizing the section, this implicitly fixes the value of ρ_2 . For a given value of H^* , the set of accessible coordinates (θ_1, ρ_1) may be significantly smaller than the natural domain $\theta_1 \in S^1, |\rho_1| \leq \rho_2$.

Reducing the dynamics from system (2.1) to system (2.5) and then to the Poincaré section in two dimensions increases the density of information in the figure. Complete understanding of the two-vortex dynamics, implied by the Poincaré section, requires “undoing” the corresponding reductions. For $H \geq H(\vec{x}_Y)$, the Poincaré map has a fixed point $(\theta_1, \rho_1) = (0, 0)$ which corresponds to the unstable fixed point \vec{x}_Y when $H = H(\vec{x}_Y)$ and to a periodic orbit surrounding it otherwise, corresponding to the periodic orbits of Figure 2(a) with the orientation of the plot rotated by 90° . These fixed points are always unstable, as is \vec{x}_Y . For $H \geq H(\vec{x}_X)$, the Poincaré map has a fixed point at $(\pi, 0)$ corresponding to the stable equilibrium \vec{x}_X at $H = H(\vec{x}_Y)$ and the periodic orbits surrounding it otherwise. As H decreases, the region of the (θ_1, ρ_1) plane accessible to intersect with physical orbits of system (2.5) shrinks. For $H < H(\vec{x}_Y)$, the fixed point at $(0, 0)$ disappears, and for $H < H(\vec{x}_X)$, the Poincaré section is empty.

Figure 7 shows four Poincaré sections computed from numerical simulations, with each set of like-colored points coming from the same computed orbit. The first three panels have $\epsilon = 0.2$. As the energy is decreased, and ρ_1 is held fixed, the accessible region of the section decreases, and for $H \lesssim 0.2245$, the accessible interval of θ_1 values does not include the entire interval $[-\pi, \pi]$ for any value of ρ_1 . Panel (a) shows $H = 0.2246$ just above $H(\vec{x}_Y)$. The Poincaré section looks like a perturbed pendulum phase plane, consistent with the reduction

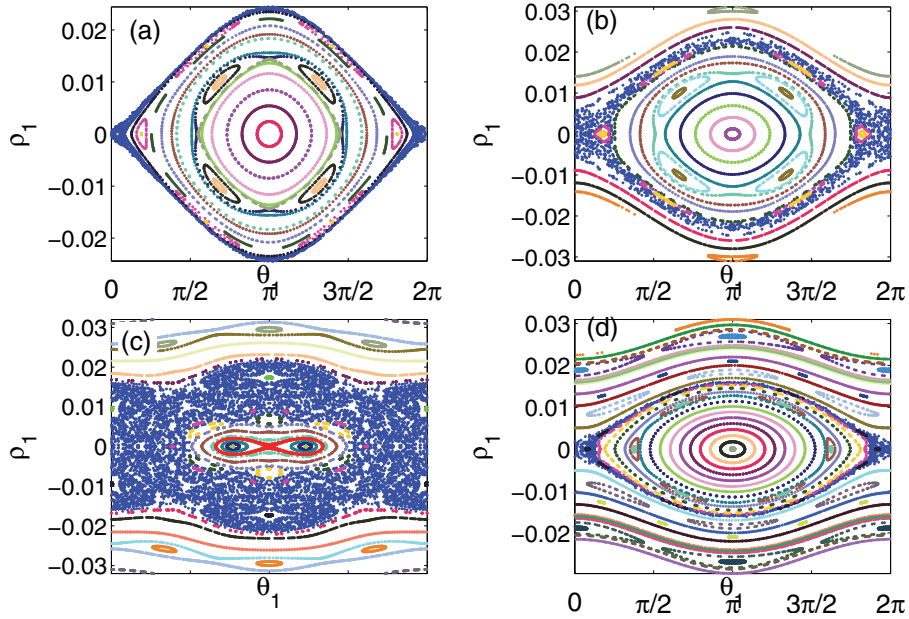


Figure 7. The Poincaré sections on the hyperplane $\theta_2 \equiv \pi \bmod 2\pi$ with parameter $B = 0.22$ in all sections and $\epsilon = 0.2$ in all but panel (d), where $\epsilon = 0.1$. The sections lie on the energy levels (a) $H = 0.2246$, (b) $H = 0.23$, (c) $H = 0.3$, and (d) $H = 0.23$. The value of H restricts the allowable values of ρ_1 , which is easily seen in all panels but (c).

to (4.2), and the accessible region contains the interior and a small portion of the exterior to the pendulum separatrix. There is a thin region of chaotic dynamics, in blue, containing the separatrix, and several families of period- n points, surrounded by quasi-periodics, can be seen, most notably a period-4 orbit and a period-6 orbit. As H is increased in the next two panels, the stochastic layer grows, until in panel (c) when the underlying pendulum dynamics is difficult to discern. More interesting in that panel is the bowtie-shaped region, plotted in red, containing the fixed point $(\pi, 0)$. What appears to be a curve having nonzero thickness is actually a narrow band of chaotic trajectories. This point corresponds to a periodic orbit surrounding \vec{x}_X . As H is increased, this periodic orbit undergoes a pitchfork bifurcation, and for energies above this bifurcation value, the periodic orbits are unstable. The critical value of H at which this instability arises could be found numerically by computing the Floquet multipliers of this family of periodic orbits. Finally, panel (d), which lies on the same energy level as (b), but with a smaller anisotropy ϵ , has smaller stochastic zones and more regular dynamics, as is to be expected.

5.3. Bifurcations in the discrete map approximation. The separatrix map (4.8) approximates the ODE dynamics in a neighborhood of the separatrix visible in Figure 7, although it is based on a different method of reduction. Using the same values of B and ϵ , we include a partial bifurcation diagram for the map (4.8) in Figure 8, computed using the MATLAB continuation package MATCONT [5]. It shows five branches of fixed points, which are real-valued following (4.9). The most salient feature of this diagram is the separatrix curve \mathcal{S} given

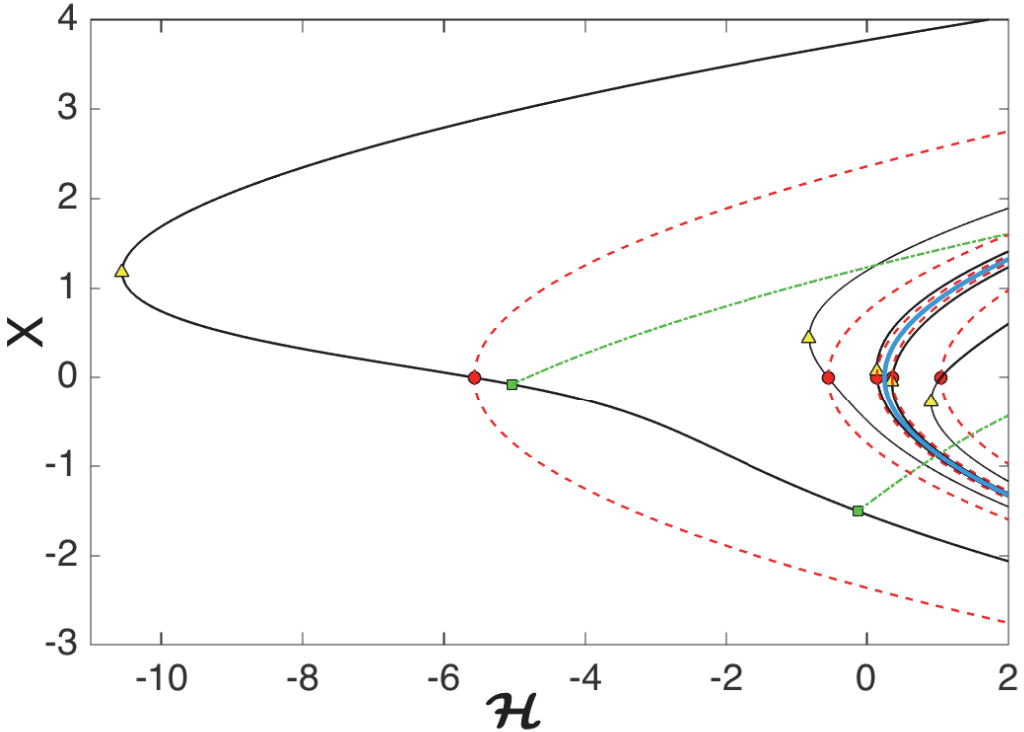


Figure 8. A partial bifurcation diagram for map (4.8). It shows the separatrix curve \mathcal{S} (light blue), fixed point branches (black line), type-1 period-two points (green dash-dot line, real parts only), type-2 period-two points (red dashed line), saddle node bifurcations (yellow triangles), type-1 period-doubling points (green squares), and type-2 period-doubling points (red circles).

by $\mathcal{H} = X^2 + \frac{1}{4}$, plotted with a light blue line. The fixed points form two countable families of branches that accumulate along \mathcal{S} from both sides. In addition, there are more solution branches lying outside the curve \mathcal{S} that cannot be considered physical because they sit too far from the separatrix to justify the assumption (4.1) under which the map was derived. Points inside the parabola correspond to orbits of system (4.3) lying *outside* the pendulum separatrix and points outside the parabola to orbits *inside* the separatrix.

We also plot some of the branches of period-two orbits described in section 4.4. The type-1 periodic orbits are complex-valued but arise in period-doubling bifurcations of real-valued fixed points. The type-2 fixed points are real and bifurcate wherever a branch of fixed points crosses the axis $X = 0$. The form of the exact period-two points shows that there are no orbits that move from the inside of the separatrix to the outside. All period-two and period-one orbits remain either on the outside, with the angle θ_2 changing monotonically, or on the inside, with the solutions remaining in an area near the stable equilibrium \vec{x}_X .

5.4. Systematic enumeration of ODE periodic orbits. The reasoning from [11] can be used to show that the separatrix map is closely connected with the Poincaré section of system (2.5) when $\theta_1 = \pi \bmod 2\pi$. The real fixed point \vec{x}_X corresponds to a periodic solution

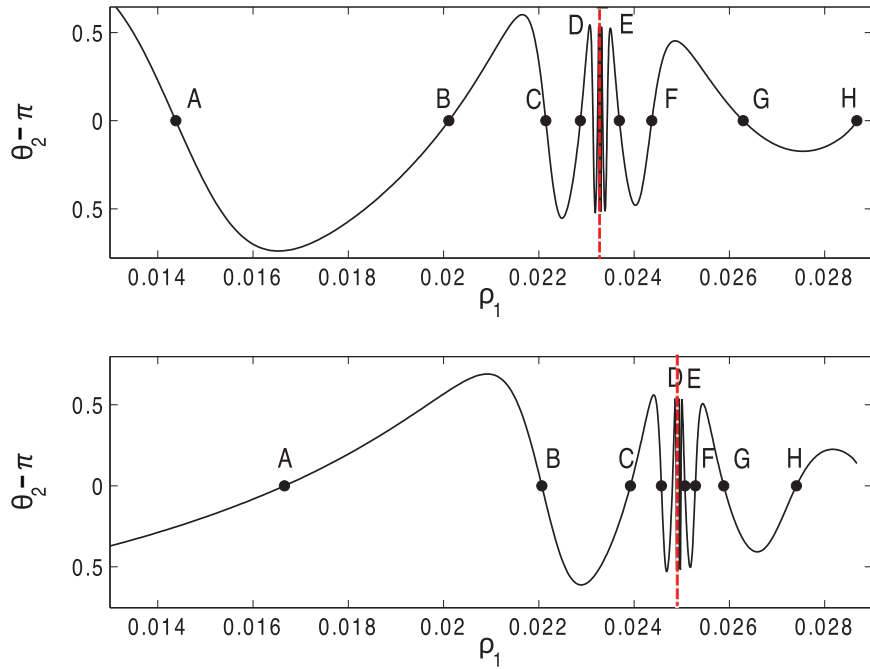


Figure 9. The value of $\theta_2(T) - \pi$ when the solution to system (2.5) is on the Poincaré section $\theta_1 = \pi$. As described in the text, zeros of this function determine symmetric periodic orbits of the system. Top: Initial condition $\rho_2(0) = \rho_2^-$. Bottom: Initial condition $\rho_2(0) = \rho_2^+$. This curve is defined for $-\rho_1^* < \rho_1 < \rho_1^*$ but is symmetric about $\rho_1 = 0$ and has no zeros on the interval $(0, 0.014)$.

for which $\theta_2 = \pi$ along this section. This leads us to the following strategy. We fix the Hamiltonian $H = H^*$ of (2.5). At this value of H^* , the action ρ_1 can take values on a finite interval $[-\rho_1^*, \rho_1^*]$. This interval is empty for H^* below some critical value. We numerically sweep through values of ρ_1 , following solutions of system (2.5) with initial conditions $\theta_1 = \theta_2 = \pi$ and ρ_2 chosen to make $H = H^*$. For each $\rho_1 \in (-\rho_1^*, \rho_1^*)$, there exist two such values of ρ_2 . Call them ρ_2^+ and ρ_2^- , and assume that $\rho_1 < \rho_2^- < \rho_2^+$. We run the ODE simulation until $\theta_1 = \pi \bmod 2\pi$. If, at this point, $\theta_2 = \pi$, then the numerical solution represents one half of a periodic orbit. In the (x_j, y_j) coordinates, these solutions have $y_1(0) = y_2(0) = 0$ and $x_1(0) \cdot x_2(0) < 0$.

We present the results of this experiment beginning in Figure 9, which shows the output value of θ_2 . The top panel shows the results with $\rho_2(0) = \rho_2^+$, and the bottom panel has $\rho_2(0) = \rho_2^-$. These curves oscillate infinitely often as ρ_1 approaches $\rho_c^- \approx 0.0233$ in the upper panel and $\rho_c^+ \approx 0.0249$ in the lower. The energy level H^* has been chosen large enough such that the branch crosses the critical curve \mathcal{S} in the bifurcation diagram. Thus, it has infinitely many real fixed points and two types of periodic orbits: rotations, which lie to the right of ρ_c , and librations, which lie to the left of ρ_c .

Figure 10 shows periodic orbits with initial condition ρ_2^- . Panels A–D show librations, and panels E–H show rotations. Plotted on these same axes are the places where the numerical solution intersects the Poincaré section. As we move from solution to solution with $\rho_1 \rightarrow \rho_c^-$,

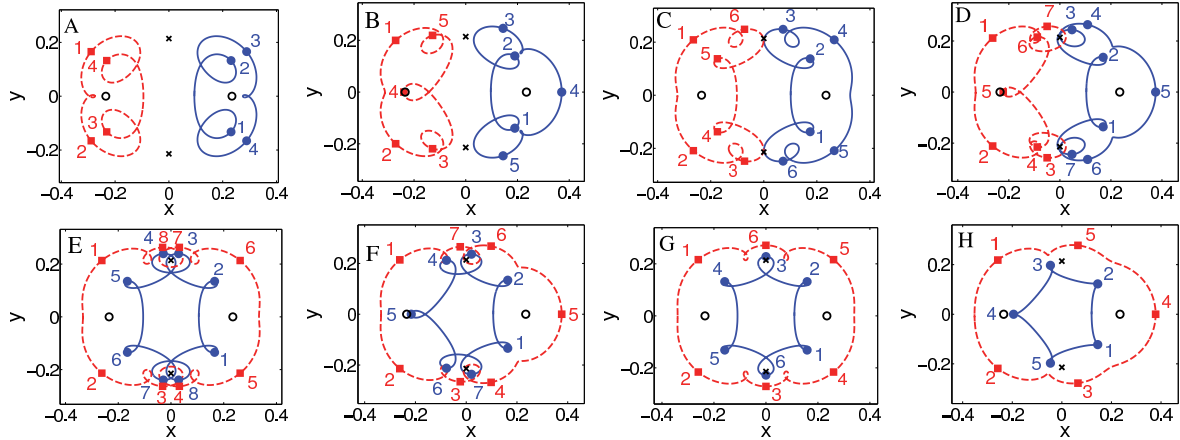


Figure 10. Periodic orbits of system (2.5) with $H^* = 0.228$ and the larger value of ρ_2 chosen as the initial condition. Note the ρ_1 -interval on which this is defined is about $[-0.029, 0.029]$, but the curve is symmetric about zero and has no roots between $\rho_1 = 0$ and the intersections marked “A” (see Figure 9). The points depicted by the black empty circles and crosses correspond to the two pairs of vortex dipole steady state solutions of equation (2.3).

the number of intersections with the θ_2 increases by one at each step, and similarly as $\rho_1 \rightarrow \rho_c^+$. The period of the orbit and the number of intersections diverge in this limit. In simulations where ρ_1 is chosen closer to ρ_c (not shown), the trajectories spend more and more time close to the unstable fixed points.

In panels A, C, E, and G, the number of points of intersection is even, while in the other four, the number of intersections is odd. In the librations with an even number of intersections (A and G), the two vortices execute orbits that are identical up to a 180° rotation and a 180° phase shift. These orbits correspond to fixed points (4.9) of the map (4.8). Periodic orbits with odd numbers correspond to real period-two points of the same map. For these orbits, the trajectories of the two vortices differ substantially.

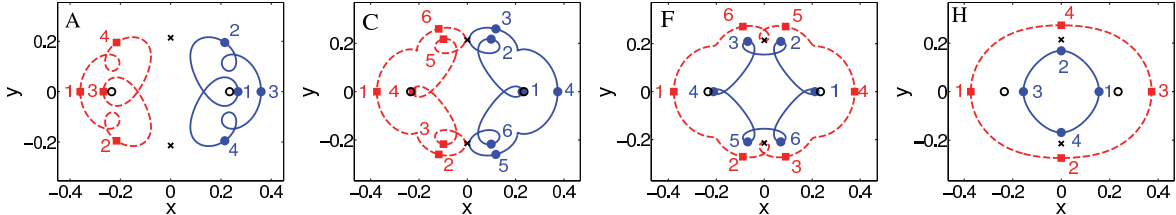


Figure 11. The solutions with initial condition ρ_2^+ . Only those that intersect the Poincaré section an even number of times are shown.

Figure 11 shows the same picture for initial conditions with initial condition ρ_2^+ . All the comments about the previous figure apply here. We have not plotted the solutions with an odd number of intersections, which include panels similar to those shown in the previous figure, up to interchanging the vortices or reflecting the figures across the y -axis. In particular, 10B \leftrightarrow 11B, 10D \leftrightarrow 11D, 10F \leftrightarrow 11E, and 10H \leftrightarrow 11G.

Of interest is how the picture changes as the energy surface $H = H^*$ is varied. As H^* is decreased, the value ρ_c moves toward the right endpoint of the interval at ρ_* . To the right of ρ_c are the rotational periodic orbits, and these get pushed out of the allowable interval starting with those that have a small number of Poincaré intersections. Eventually, the accumulation point ρ_c exits, too, eliminating all the rotational motions. Then, the librations with large numbers of Poincaré intersections disappear, followed by those with small numbers of intersections. So, for example, when $H = 0.223$, only the solutions corresponding to A, B, and C in Figure 9 remain.

Conversely, by increasing H , additional rotational orbits bifurcate in from the right endpoint. In fact, some libratory orbits bifurcate from $\rho_1 = 0$. Figure 12 shows four additional periodic orbits that exist for $H = 0.3$ but not for $H = 0.228$, which is plotted above. One of these has two Poincaré intersections, two more have three, and a fourth has four. The last one is included for comparison with the PDE simulations of the next section.

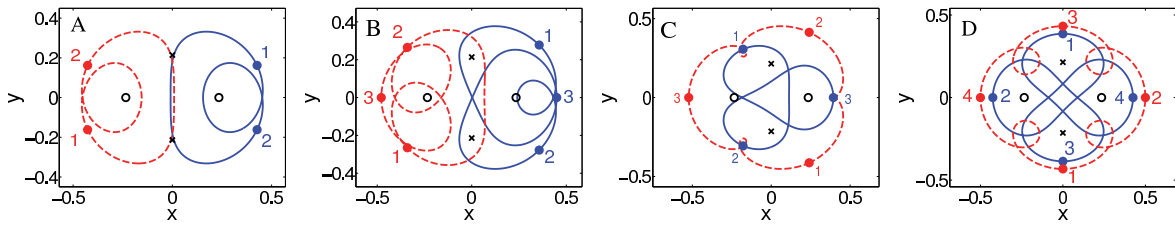


Figure 12. Periodic vortex paths corresponding with Hamiltonian $H = 0.3$, with fewer Poincaré sections than seen in previous figure.

6. Numerical solutions to the GP equation. In this section we corroborate the results obtained from the reduced system of ODEs (2.1) for the original GP equation (1.1), showcasing in this way that the relevant periodic orbits identified by the map approach, albeit of considerable complexity, are especially relevant for observation in experimentally accessible BEC settings. The parameter $B = 0.22$ used in the previous sections was earlier used to theoretically mirror the experimental dynamics of an isotropic BEC containing approximately 500,000 ^{87}Rb atoms trapped in the radial and axial directions with trap frequencies $(\omega_r, \omega_z)/(2\pi) = (35.8, 101.2)\text{Hz}$ [39]. These values for the physical parameters translate into a GP equation (1.1) with the effective quasi-two-dimensional (isotropic) potential

$$(6.1) \quad V(x, y) = \frac{1}{2} \left(\frac{\omega_r}{\omega_z} \right)^2 r^2 = \frac{1}{2} \Omega^2 (x^2 + y^2)$$

with an effective trap strength of $\Omega = \omega_r/\omega_z = 0.3538$ and an adimensional chemical potential $\mu = 16.69$ so that the stationary state solution, $v(x, y)$, for (1.1) can be written as $u(x, y, t) = v(x, y)e^{-i\mu t}$. We introduce the anisotropy in the potential by replacing the potential in (6.1) by

$$(6.2) \quad V(x, y) = \frac{1}{2} \Omega^2 [x^2 + (1 + \epsilon)y^2],$$

where the anisotropy parameter ϵ corresponds to (a) $\epsilon = 0$ for the isotropic case and (b) $\epsilon = 0.2$ for the anisotropic case studied in the previous sections.

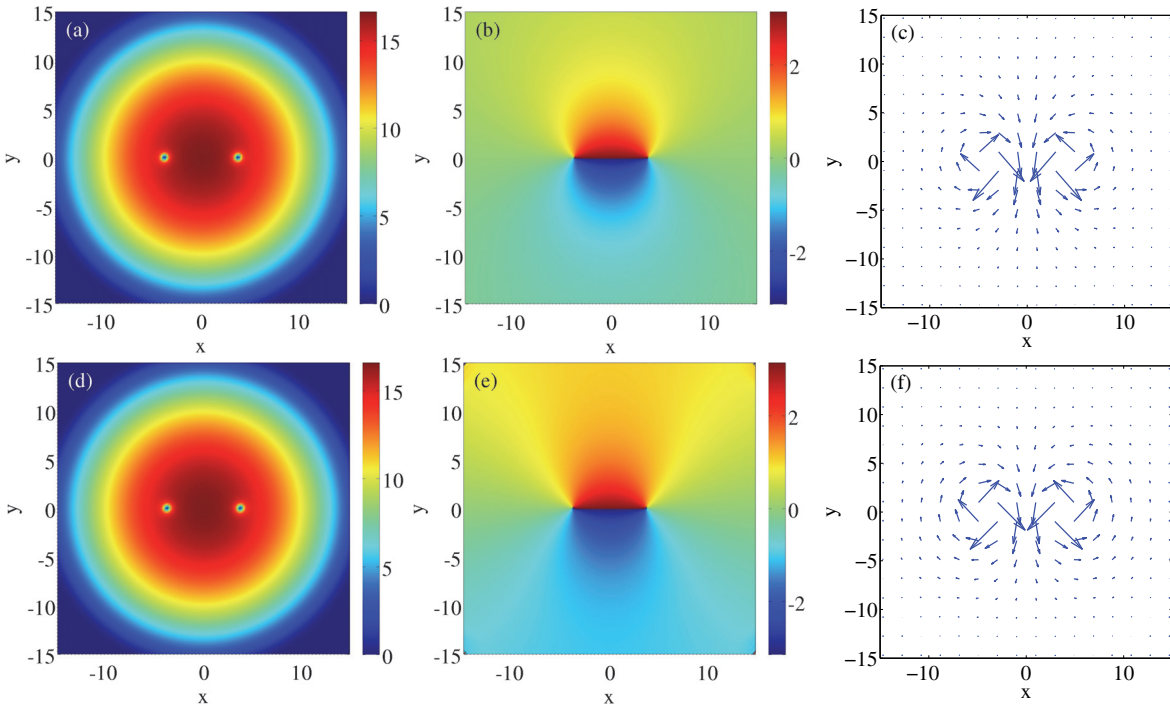


Figure 13. Steady state dipole configurations. The top row depicts (a) density, (b) phase, and (c) fluid velocity for a vortex dipole seeded, using the approximate solution (6.3), at the steady state position (2.3) on an isotropic BEC. Similarly, the bottom row depicts the actual steady state solution for the stationary vortex dipole using a Newton-type fixed point iteration method. The fluid velocity corresponds to the gradient of the phase.

To numerically investigate the dynamics of vortex dipoles in the GP equation (1.1) we first find the steady state solution, namely, the ground (vortex-free) state of the system, $v(x, y)$, by substituting $u(x, y, t) = v(x, y)e^{-i\mu t}$ into (1.1) and solving the ensuing time-independent problem with a Newton-type fixed point iterative method. Once the steady state is found, we need to seed the vortex dipole into this ground state. To do so, we first extract the vortex profile by solving the homogeneous ($V = 0$) problem (1.1) in radial coordinates (r, θ) for a vortex solution of charge $S = 1$ centered at the origin: $u(r, \theta, t) = f(r)e^{-i\mu t}e^{iS\theta}$. The ensuing boundary value problem with boundary values $f(r = 0) = 0$ and $f(r = \infty) = \sqrt{\mu}$ is numerically solved using the standard boundary value problem solver `bvp4c` in MATLAB. Now, equipped with the numerically exact radial profile $f(r)$, we proceed to imprint a vortex of charge $S = \pm 1$ at any desired location $\mathbf{r}_0 = (x_0, y_0)$ within the BEC by multiplying the steady solution $v(x, y)$ found above by a normalized vortex profile:

$$(6.3) \quad u_0(x, y) = v(x, y) \times \frac{f(\mathbf{r} - \mathbf{r}_0)}{\sqrt{\mu}} \times e^{-iS\theta_0},$$

where θ_0 is the polar angle of any point (x, y) within the BEC measured from the center of the vortex (x_0, y_0) . This initial condition provides a vortex configuration that is very close to the exact profile. Our approximation relies on the assumption that the background profile for the

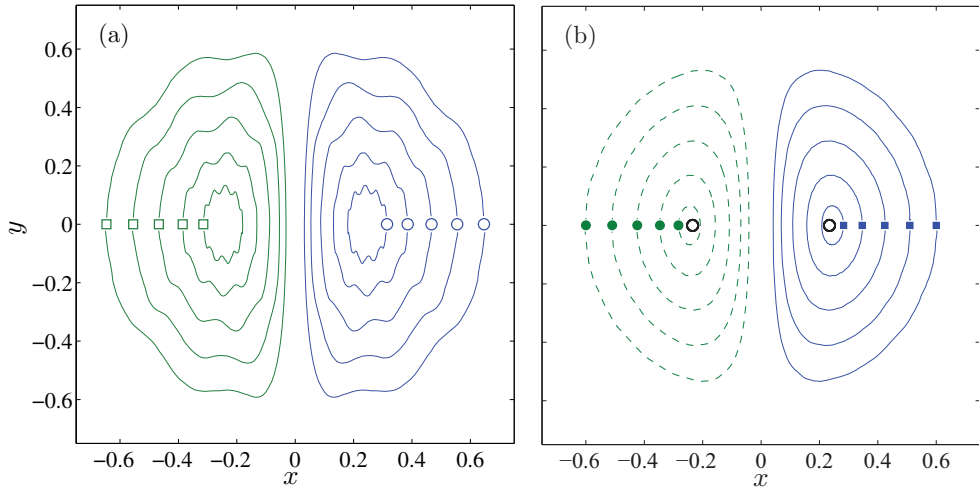


Figure 14. (a) *Orbits generated by the full GP dynamics of a vortex dipole seeded in the BEC using (6.3).* The orbits are similar to those obtained using the ODE reduction as in Figure 2a. However, notice the spurious “wiggles” present in all GP dynamics. (b) *Corresponding orbits after subtracting the linear momenta of the initial configuration (6.3).* Note that the wiggles are no longer present.

steady state varies slowly over the vortex core size. In this manner, our approximation using the homogeneous background yields a close approximation to the actual vortex profile that sheds very little radiation when numerically integrated. It is worth mentioning at this stage that the typical vortex width for the GP numerics (and the associated laboratory experiment described in [39]) is small ($\approx 1/30$ th) compared to the width of the BEC cloud (see, for example, the two vortices in the left panels of Figure 13).

The top row of panels in Figure 13 shows, respectively, from left to right, the density, phase, and fluid velocity associated with a vortex dipole initiated, using the above method, at the steady state positions (2.3) on an isotropic ($\epsilon = 0$) BEC. Seeding the GP numerics using the approximate solution (6.3) has an unexpected spurious effect, as can be observed from the extracted vortex orbits depicted in Figure 14(a). The figure shows, contrary to the smooth orbits from the effective ODE dynamics depicted in Figure 2, spurious up-down “wiggles.” Close inspection of these wiggles reveals that they originate from an undesired perturbation of the sloshing (back-and-forth) mode of the steady state background. This can be confirmed by comparing the seeded solution using (6.3) to the true steady state when the dipole is placed at the fixed point (2.3). The bottom panels of Figure 13 depict, respectively, the density, phase, and fluid velocity of the true steady state dipole found through a Newton-type fixed point iteration method. It is interesting to compare our approximate seeded solution (top panels) to the numerical exact solution (bottom panels). In fact, the density and fluid velocity seem quite close for both cases. However, it is evident that the phase distribution is indeed different. To elucidate the effects of the discrepancy between these two configurations, we depict their differences in Figure 15. The panels correspond to the difference between (a) the phases and (b) the fluid velocities. As is clear from this figure, the phase difference between the two cases shows a clear vertical gradient (see Figure 15(a)) that, in turn, is reflected in a vertical fluid

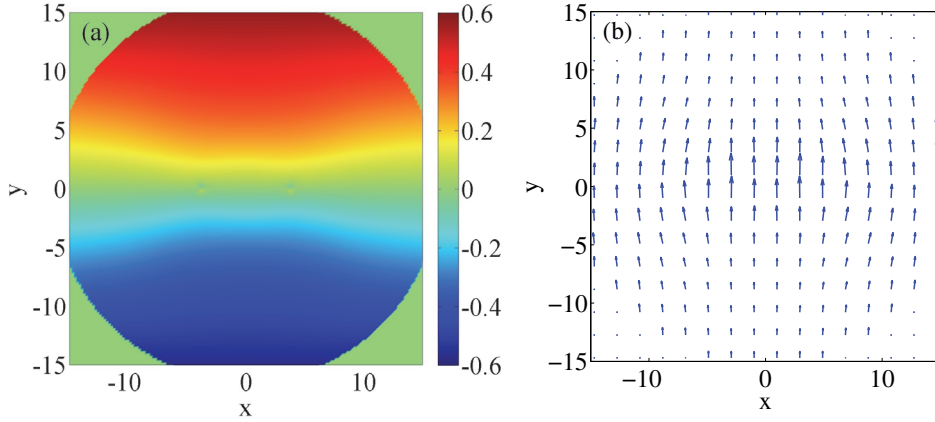


Figure 15. Difference between the steady state dipole vortex configuration seeded using (6.3) (see top row of panels of Figure 13) and the numerically exact solution (see bottom row of panels of Figure 13). Panels (a) and (b) depict, respectively, the difference between the phases and the fluid velocities.

velocity (see Figure 15(b)). This upward fluid velocity is then responsible for perturbing the sloshing (up-down) mode of the background cloud, resulting in the spurious wiggles present in the orbits depicted in Figure 14(a).

Having detected the origin of the spurious wiggles when naively using the seed given by (6.3), we proceed to remove the effects of the undesired perturbation of the sloshing mode. A possible way to eliminate the sloshing from the dynamics is to use initial conditions in which the projection of the ground state onto the sloshing mode is subtracted. This would require us to obtain the eigenfunctions of the linearized steady state (ground state) configuration. Instead, we opt here to use a simpler and more direct method. We simply compute the linear momenta, in both x and y , of the seeded initial vortex configuration and imprint the opposite momenta into the initial configuration to cancel any possible sloshing. Thus, after obtaining the desired combination of seeded vortices using (6.3), we compute the linear momenta,

$$P_z = i \iint \left(u_0 \frac{d\bar{u}_0}{dz} - \bar{u}_0 \frac{du_0}{dz} \right) dx dy,$$

where z needs to be replaced by x or y for the respective horizontal and vertical linear momenta. Then, the “distilled” initial configuration is obtained by adding the corresponding opposite momenta to cancel any residual linear momenta that may be responsible for the appearance of the sloshing mode, i.e.,

$$u_{\text{ini}} = u_0 \times e^{ik_x x} \times e^{ik_y y},$$

where the “kicks” k_x and k_y are chosen so that the new linear momenta of u_{ini} are zero. The advantage of using this method is that, in principle, it works for any vortex configuration with any number of vortices. In Figure 14(b) we depict the corresponding orbits after removal of the spurious sloshing mode. As is clear from the figure, the spurious wiggles are no longer present since we are no longer perturbing the sloshing mode. From now on we use the above subtraction of the sloshing mode for all the seeding of our initial vortex dipole configurations in the GP model.

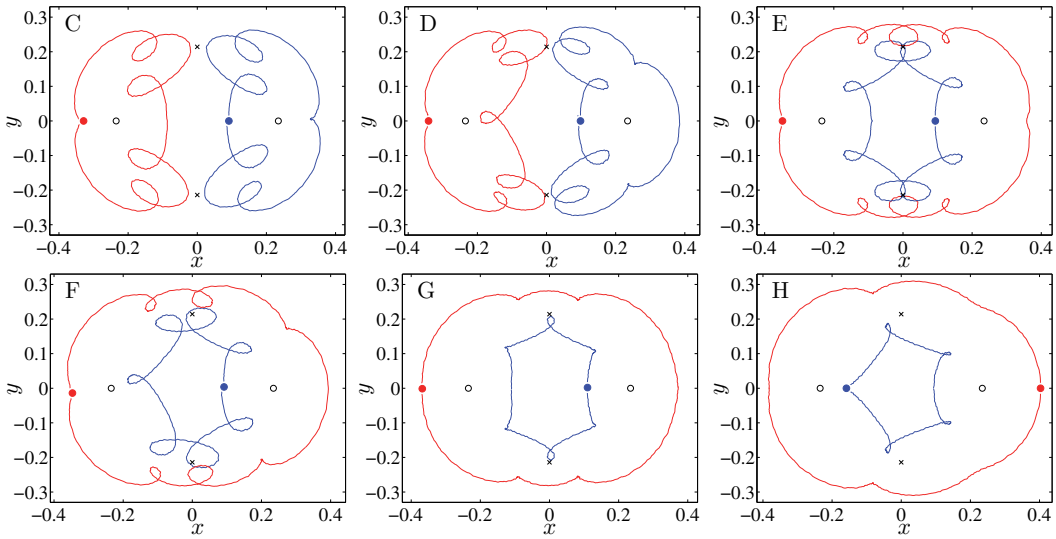


Figure 16. Periodic orbits of the full GP model (1.1) with an anisotropic potential (6.2) with $\epsilon = 0.2$. The initial conditions were found by using the initial conditions corresponding to the periodic orbits of the reduced ODE system (2.1) as seeds for a local search in initial condition space (see text for details). The different panels are labeled using the same notation as the respective panels in Figure 10 and the top panel of Figure 9, namely, for an energy of $H = 0.228$.

We now proceed to find the periodic orbits on the full GP model (1.1) corresponding to the ODE orbits described in the previous section. It is important to mention that since the ODE reduction for a vortex dipole is an approximation of the corresponding full GP dynamics, initial conditions yielding periodic orbits for the ODE model do not exactly correspond to initial conditions yielding periodic orbits of the full GP model. However, since the ODE reduction provides a reasonable approximation, we use the initial conditions corresponding to periodic orbits for the ODE as starting seeds for a local (in initial condition space) search of the full GP periodic orbits. The local search for initial conditions (x_1, y_1, x_2, y_2) corresponding to periodic orbits is carried by setting $y_1 = y_2 = 0$ and performing a local two-dimensional parameter sweep in (x_1, x_2) space around the corresponding ODE initial condition. In this manner, using a 10×10 grid in (x_1, x_2) space with a width of 0.01, we are able to find approximate periodic orbits for the full GP model. In some instances, a second parameter sweep on a new 10×10 grid with spacing 0.001, centered about the most promising initial condition of the previous grid, was used to refine the initial condition for better convergence to the periodic orbit. The resulting periodic orbits of the full GP model are depicted in Figures 16–18. The depicted orbits correspond, respectively, to most of the ODE periodic orbits depicted in Figures 10–12, including both librations (such as C and D) and rotations (such as E–H). As is clear from the figures, the periodic orbits of the reduced ODE model, found with the Poincaré sections described in the previous section, have equivalent orbits in the original GP model. It is remarkable that such a reduction is able to capture these types of complex periodic orbits, revealing their numerous twists which are in turn associated, as indicated in the previous section, to their number of intersections with the Poincaré section.

Finally, to highlight the correspondence between the full GP dynamics and the reduced

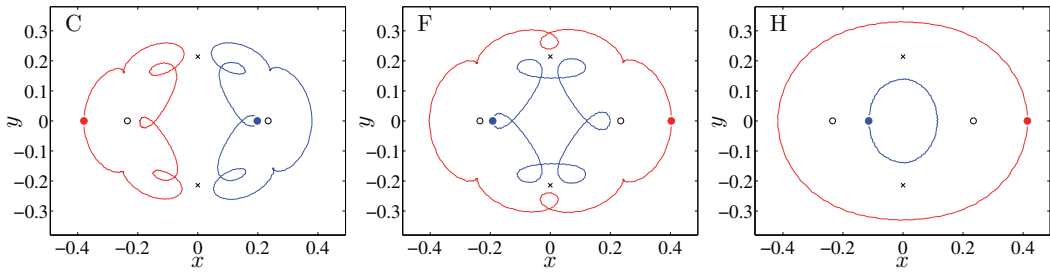


Figure 17. Same as in Figure 17 for the respective panels of Figure 11 and the bottom panel of Figure 9. Namely, for an energy of $H = 0.228$.

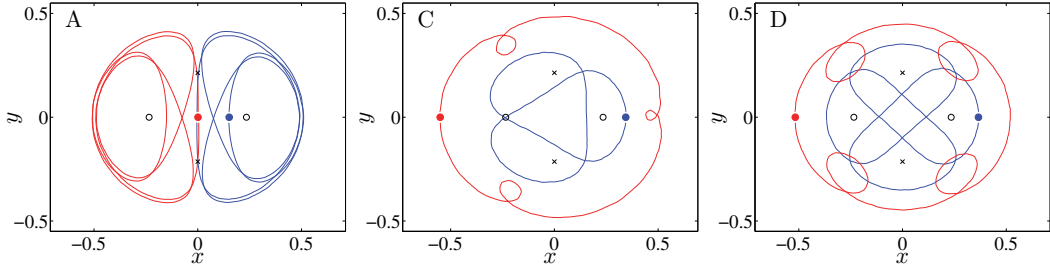


Figure 18. Same as in Figure 18 for the respective panels of Figure 12. Namely, for an energy of $H = 0.3$.

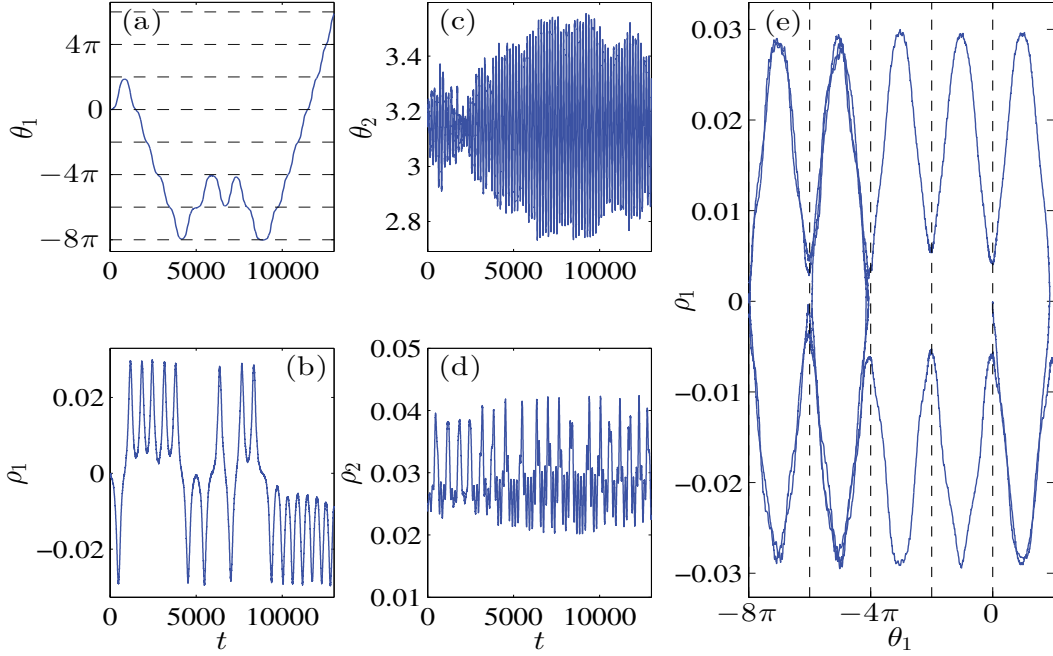


Figure 19. Same as in Figure 6 but for the full GP model (1.1). Same layout and notation as in Figure 6.

ODE model, we searched for initial conditions, using the seeding and the local search method explained above, that reproduce the chaotic behavior observed near the unstable guiding-

center fixed point displaying a pendulum separatrix-type behavior (see Figure 6). An example of this behavior for the full GP model is depicted in Figure 19 using the same layout as in Figure 6. As the figure shows, there is a striking similarity between the reduced ODE dynamics and the original PDE model, including the chaotic switching between left and right rotations, the relation between the sign of ρ_1 and the rotational direction of θ_1 , and the overall proximity of the (ρ_1, θ_1) plane to the corresponding pendulum separatrix.

7. Discussion. While previous studies have chiefly focused on the fixed point type orbits of a vortex dipole (and their linear stability) in an anisotropic trap, we have used techniques of Hamiltonian mechanics to explore, in a detailed way, the dynamics of such an anisotropic system. Arguably, this is one of the simplest vortex systems where the lack of integrability can be seen to be responsible for complex and chaotic dynamics in addition to periodic and quasi-periodic orbits. In the process, we have discovered and enumerated a large number of families of periodic orbits and regions of chaotic dynamics.

This approach should be useful in uncovering the dynamics of many related systems. A straightforward example would be to change the sign of one of the vortices to make them corotating. This has been considered for the case of an isotropic trap in [19, 39, 60]. The isotropic case shows more interesting dynamics than what was shown in section 3 of the present case, including pitchfork bifurcations leading to asymmetric time-dependent motions (although these are critically seeded by the radial dependence of the precession frequency not considered herein). How such dynamics interacts with an imposed anisotropy would be an interesting follow-up question. While this theme has already been touched upon in the physics community [32, 33], it still lacks a systematic characterization based on the techniques presented above.

The isotropic examples of the corotating [39] and of the counterrotating [34] dipoles have been experimentally explored. Yet, it should be especially interesting to look for the behavior found here in similar laboratory experiments. This may not be easy. The imaging procedure used in the experiments causes the atom number to decrease over time (as a small fraction is transferred to a different hyperfine state in order to be imaged). Consequently, a more realistic model of the motion may include dissipation which, in turn, has a nontrivial impact on the dynamics, leading individual vortices to a spiraling out (rather than rotational) motion; see, e.g., the recent discussion of [59] and references therein. Additionally, many of the phenomena described require a long time series, and the time series obtainable in the laboratory experiments may be too short to observe them.

The related system consisting of three vortices and an isotropic trap, either with all three corotating or else with one vortex of opposite sign, is known from numerical experiments to exhibit chaotic dynamics [4], and an attempt has been made to understand these systems using finite-dimensional reductions and index-based tools that enable the quantification of the potential chaoticity of the orbits [20, 23]. For systems with more vortices, the reductions carried out here may be less helpful as the number of dimensions in the reduced system may still be too large to say very much about. In addition, such systems may lack the small parameter necessary to apply perturbation methods. Here, the energy-momentum bifurcation diagram, as applied in [51], may be a useful tool, as might symmetry-based methods [1, 35, 36, 37].

In general, there exists a wide body of literature in nonlinear waves looking at special solutions, such as periodic orbits and solitary waves, and examining their stability. Much of this work makes the implicit assumption that only stable solutions are experimentally important, since unstable solutions would be unobservable in practice. This is contrary to the lessons from finite-dimensional dynamical systems that unstable solutions are important because their stable and unstable manifolds separate regions of phase space and provide skeletons that organize the dynamics, as we have also seen in this paper. There is a more recent trend recognizing this fact and exploring related phenomena in nonlinear wave systems (see, e.g., [12, 15, 30, 43]), and there exist many problems which might be further understood using such an approach. However, again an emerging crucial step will be the ability to overcome the limitation of very low-dimensional systems; e.g., in the realm of vortices, it is especially relevant to build a progressive understanding of small or intermediate clusters of (3 or 4 and up to 11 or so [39]) vortices and even of larger clusters in the form of vortex lattices [47], which are of particular experimental interest.

REFERENCES

- [1] T. BOUNTIS, G. CHECHIN, AND V. SAKHNENKO, *Discrete symmetry and stability in Hamiltonian dynamics*, Internat. J. Bifur. Chaos Appl. Sci. Engrg., 21 (2011), pp. 1539–1582.
- [2] R. CAMASSA, G. KOVACIC, AND S. K. TIN, *A Melnikov method for homoclinic orbits with many pulses*, Arch. Ration. Mech. Anal., 143 (1998), pp. 105–193.
- [3] Y. CASTIN AND R. DUM, *Bose-Einstein condensates with vortices in rotating traps*, Eur. Phys. J. D, 7 (1999), pp. 399–412.
- [4] S. M. CHANG, W. W. LIN, AND T. C. LIN, *Dynamics of vortices in two-dimensional Bose-Einstein condensates*, Internat. J. Bifur. Chaos Appl. Sci. Engrg., 12 (2002), pp. 739–764.
- [5] A. DHOOGE, W. GOVAERTS, AND Y. A. KUZNETSOV, *MATCONT: A MATLAB package for numerical bifurcation analysis of ODEs*, ACM Trans. Math. Software, 29 (2003), pp. 141–164.
- [6] A. L. FETTER AND A. A. SVIDZINSKY, *Vortices in a trapped dilute Bose-Einstein condensate*, J. Phys. Condens. Matt., 13 (2001), pp. R135–R194.
- [7] A. L. FETTER, *Rotating trapped Bose-Einstein condensates*, Rev. Modern Phys., 81 (2009), pp. 647–691.
- [8] A. L. FETTER, *Vortex dynamics in spin-orbit-coupled Bose-Einstein condensates*, Phys. Rev. A, 89 (2014), 023629.
- [9] D. V. FREILICH, D. M. BIANCHI, A. M. KAUFMAN, T. K. LANGIN, AND D. S. HALL, *Real-time dynamics of single vortex lines and vortex dipoles in a Bose-Einstein condensate*, Science, 329 (2010), pp. 1182–1185.
- [10] H. GOLDSTEIN, C. POOLE, AND J. SAFKO, *Classical Mechanics*, 3rd ed., Addison Wesley, Reading, MA, 2001.
- [11] R. H. GOODMAN, *Chaotic scattering in solitary wave interactions: A singular iterated-map description*, Chaos, 18 (2008), 023113.
- [12] R. H. GOODMAN, *Hamiltonian Hopf bifurcations and dynamics of NLS/GP standing-wave modes*, J. Phys. A., 44 (2011), 425101.
- [13] R. H. GOODMAN AND R. HABERMAN, *Kink-antikink collisions in the ϕ^4 equation: The n-bounce resonance and the separatrix map*, SIAM J. Appl. Dyn. Syst., 4 (2005), pp. 1195–1228.
- [14] R. H. GOODMAN AND R. HABERMAN, *Chaotic scattering and the n-bounce resonance in solitary-wave interactions*, Phys. Rev. Lett., 98 (2007), 104103.
- [15] R. H. GOODMAN, J. L. MARZUOLA, AND M. I. WEINSTEIN, *Self-trapping and Josephson tunneling solutions to the nonlinear Schrödinger/Gross-Pitaevskii equation*, Discrete Contin. Dyn. Syst. A, 35 (2015), pp. 225–246.
- [16] P. HOLMES, *Poincaré, celestial mechanics, dynamical-systems theory and “chaos”*, Phys. Rep., 193 (1990), pp. 137–163.

- [17] R. L. JERRARD AND D. SMETS, *Vortex dynamics for the two dimensional non homogeneous Gross-Pitaevskii equation*, arxiv preprint, 1301.5213, <http://arxiv.org/abs/1301.5213>, 2013.
- [18] P. G. KEVREKIDIS, D. J. FRANTZESKAKIS, AND R. CARRETERO-GONZÁLEZ, *Emergent Nonlinear Phenomena in Bose-Einstein Condensates*, Springer-Verlag, Heidelberg, 2008.
- [19] T. KOLOKOLNIKOV, P. G. KEVREKIDIS, AND R. CARRETERO-GONZÁLEZ, *A tale of two distributions: From few to many vortices in quasi-two-dimensional Bose-Einstein condensates*, Proc. R. Soc. Lond. Ser. A. Math. Phys. Eng. Sci., 470 (2014), 20140048.
- [20] V. KOUKOLOYANNIS, G. VOYATZIS, AND P. G. KEVREKIDIS, *Dynamics of three noncorotating vortices in Bose-Einstein condensates*, Phys. Rev. E, 89 (2014), 042905.
- [21] P. KUOPANPORTTI, J. A. M. HUHTAMÄKI, AND M. MÖTTÖNEN, *Size and dynamics of vortex dipoles in dilute Bose-Einstein condensates*, Phys. Rev. A, 83 (2011), 011603.
- [22] M. KURZKE, C. MELCHER, R. MOSER, AND D. SPIRN, *Dynamics for Ginzburg-Landau vortices under a mixed flow*, Indiana Univ. Math. J., 58 (2009), pp. 2597–2621.
- [23] N. KYRIAKOPOULOS, V. KOUKOLOYANNIS, C. SKOKOS, AND P. G. KEVREKIDIS, *Chaotic behavior of three interacting vortices in a confined Bose-Einstein condensate*, Chaos, 24 (2014), 024410.
- [24] A. E. LEANHARDT, A. GöRLITZ, A. P. CHIKKATUR, D. KIELPINSKI, Y. SHIN, D. E. PRITCHARD, AND W. KETTERLE, *Imprinting vortices in a Bose-Einstein condensate using topological phases*, Phys. Rev. Lett., 89 (2002), 190403.
- [25] W. LI, M. HAQUE, AND S. KOMINEAS, *Vortex dipole in a trapped two-dimensional Bose-Einstein condensate*, Phys. Rev. A, 77 (2008), 053610.
- [26] A. J. LICHTENBERG AND M. A. LIEBERMAN, *Regular and Chaotic Dynamics*, Springer-Verlag, New York, 1992.
- [27] E. N. LORENZ, *On the existence of a slow manifold*, J. Atmospheric Sci., 43 (1986), pp. 1547–1557.
- [28] K. W. MADISON, F. CHEVY, V. BRETN, AND J. DALIBARD, *Stationary states of a rotating Bose-Einstein condensate: Routes to vortex nucleation*, Phys. Rev. Lett., 86 (2001), pp. 4443–4446.
- [29] K. W. MADISON, F. CHEVY, W. WOHLLEBEN, AND J. DALIBARD, *Vortex formation in a stirred Bose-Einstein condensate*, Phys. Rev. Lett., 84 (2000), pp. 806–809.
- [30] J. L. MARZUOLA AND M. I. WEINSTEIN, *Long time dynamics near the symmetry breaking bifurcation for nonlinear Schrödinger/Gross-Pitaevskii equations*, Discrete Contin. Dyn. Syst. A, 28 (2010), pp. 1505–1554.
- [31] M. R. MATTHEWS, B. P. ANDERSON, P. C. HALJAN, D. S. HALL, C. E. WIEMAN, AND E. A. CORNELL, *Vortices in a Bose-Einstein condensate*, Phys. Rev. Lett., 83 (1999), pp. 2498–2501.
- [32] S. MCENDOO AND T. BUSCH, *Small numbers of vortices in anisotropic traps*, Phys. Rev. A, 79 (2009), 053616.
- [33] S. MCENDOO AND TH. BUSCH, *Vortex dynamics in anisotropic traps*, Phys. Rev. A, 82 (2010), 013628.
- [34] S. MIDDELKAMP, P. J. TORRES, P. G. KEVREKIDIS, D. J. FRANTZESKAKIS, R. CARRETERO-GONZÁLEZ, P. SCHMELCHER, D. V. FREILICH, AND D. S. HALL, *Guiding-center dynamics of vortex dipoles in Bose-Einstein condensates*, Phys. Rev. A, 84 (2011), 011605.
- [35] J. A. MONTALDI, R. M. ROBERTS, AND I. N. STEWART, *Periodic solutions near equilibria of symmetric Hamiltonian systems*, Philos. Trans. Roy. Soc. London Ser. A, 325 (1988), pp. 237–293.
- [36] J. A. MONTALDI, R. M. ROBERTS, AND I. N. STEWART, *Existence of nonlinear normal modes of symmetric Hamiltonian systems*, Nonlinearity, 3 (1990), pp. 695–730.
- [37] J. A. MONTALDI, R. M. ROBERTS, AND I. N. STEWART, *Stability of nonlinear normal modes of symmetric Hamiltonian systems*, Nonlinearity, 3 (1990), pp. 731–772.
- [38] M. MÖTTÖNEN, S. M. M. VIRTANEN, T. ISOSHIMA, AND M. M. SALOMAA, *Stationary vortex clusters in nonrotating Bose-Einstein condensates*, Phys. Rev. A, 71 (2005), 033626.
- [39] R. NAVARRO, R. CARRETERO-GONZÁLEZ, P. J. TORRES, P. G. KEVREKIDIS, D. J. FRANTZESKAKIS, M. W. RAY, E. ALTUNTAŞ, AND D. S. HALL, *Dynamics of few co-rotating vortices in Bose-Einstein condensates*, Phys. Rev. Lett., 110 (2013), 225301.
- [40] T. W. NEELY, E. C. SAMSON, A. S. BRADLEY, M. J. DAVIS, AND B. P. ANDERSON, *Observation of vortex dipoles in an oblate Bose-Einstein condensate*, Phys. Rev. Lett., 104 (2010), 160401.
- [41] R. ONOFRIO, C. RAMAN, J. M. VOGELS, J. R. ABO-SHAER, A. P. CHIKKATUR, AND W. KETTERLE, *Observation of superfluid flow in a Bose-Einstein condensed gas*, Phys. Rev. Lett., 85 (2000), pp. 2228–2231.

- [42] D. E. PELINOVSKY AND P. G. KEVREKIDIS, *Variational approximations of trapped vortices in the large-density limit*, Nonlinearity, (2011), pp. 1271–1289.
- [43] D. PELINOVSKY AND T. PHAN, *Normal form for the symmetry-breaking bifurcation in the nonlinear Schrödinger equation*, J. Diff. Eq., 253 (2012), pp. 2796–2824.
- [44] C. J. PETHICK AND H. SMITH, *Bose-Einstein Condensation in Dilute Gases*, Cambridge University Press, Cambridge, UK, 2002.
- [45] L. P. PITAEVSKII AND S. STRINGARI, *Bose-Einstein Condensation*, Oxford University Press, Oxford, UK, 2003.
- [46] H. POINCARÉ, *Sur les équations de la dynamique et le problème des trois corps*, Acta. Math., 13 (1890), pp. 1–270.
- [47] C. RAMAN, J. R. ABO-SHAER, J. M. VOGELS, K. XU, AND W. KETTERLE, *Vortex nucleation in a stirred Bose-Einstein condensate*, Phys. Rev. Lett., 87 (2001), 210402.
- [48] A. RECATI, F. ZAMBELLI, AND S. STRINGARI, *Overcritical rotation of a trapped Bose-Einstein condensate*, Phys. Rev. Lett., 86 (2001), pp. 377–380.
- [49] D. R. SCHERER, C. N. WEILER, T. W. NEELY, AND B. P. ANDERSON, *Vortex formation by merging of multiple trapped Bose-Einstein condensates*, Phys. Rev. Lett., 98 (2007), 110402.
- [50] J. A. SEMAN, E. A. L. HENN, M. HAQUE, R. F. SHIOZAKI, E. R. F. RAMOS, M. CARACANHAS, P. CASTILHO, C. CASTELO BRANCO, P. E. S. TAVARES, F. J. POVEDA-CUEVAS, G. ROATI, K. M. F. MAGALHÃES, AND V. S. BAGNATO, *Three-vortex configurations in trapped Bose-Einstein condensates*, Phys. Rev. A, 82 (2010), 033616.
- [51] E. SHLIZERMAN AND V. ROM-KEDAR, *Hierarchy of bifurcations in the truncated and forced nonlinear Schrödinger model*, Chaos, 15 (2005), 013107.
- [52] Y. SINHA AND SA.ND CASTIN, *Dynamic instability of a rotating Bose-Einstein condensate*, Phys. Rev. Lett., 87 (2001), 190402.
- [53] J. STOCKHOFE, *Vortex Cluster and Dark-Bright Ring Solitons in Bose-Einstein Condensates*, Master's thesis, University of Hamburg, Hamburg, Germany, 2011.
- [54] J. STOCKHOFE, P. G. KEVREKIDIS, AND P. SCHMELCHER, *Existence, stability and nonlinear dynamics of vortices and vortex clusters in anisotropic Bose-Einstein condensates*, in Spontaneous Symmetry Breaking, Self-Trapping, and Josephson Oscillations, Progress in Optical Science and Photonics, B. Malomed, ed., Springer, New York, 2013, pp. 543–581.
- [55] J. STOCKHOFE, S. MIDDELKAMP, P. G. KEVREKIDIS, AND P. SCHMELCHER, *Impact of anisotropy on vortex clusters and their dynamics*, Eur. Phys. Lett., 93 (2011), 20008.
- [56] P. J. TORRES, P. G. KEVREKIDIS, D. J. FRANTZESKAKIS, R. CARRETERO-GONZÁLEZ, P. SCHMELCHER, AND D. S. HALL, *Dynamics of vortex dipoles in confined Bose-Einstein condensates*, Phys. Lett. A, 375 (2011), pp. 3044–3050.
- [57] C. N. WEILER, T. W. NEELY, D. R. SCHERER, A. S. BRADLEY, M. J. DAVIS, AND B. P. ANDERSON, *Spontaneous vortices in the formation of Bose-Einstein condensates*, Nature, 455 (2008), pp. 948–951.
- [58] J. E. WILLIAMS AND M. J. HOLLAND, *Preparing topological states of a Bose-Einstein condensate*, Nature, 401 (1999), pp. 568–572.
- [59] D. YAN, R. CARRETERO-GONZÁLEZ, D. J. FRANTZESKAKIS, P. G. KEVREKIDIS, N. P. PROUKAKIS, AND D. SPIRN, *Exploring vortex dynamics in the presence of dissipation: Analytical and numerical results*, Phys. Rev. A, 89 (2014), 043613.
- [60] A. V. ZAMPETAKI, R. CARRETERO-GONZÁLEZ, P. G. KEVREKIDIS, F. K. DIAKONOS, AND D. J. FRANTZESKAKIS, *Exploring rigidly rotating vortex configurations and their bifurcations in atomic Bose-Einstein condensates*, Phys. Rev. E, 88 (2013), 042914.